

1 **Object-based ensemble estimation of snow depth and snow water 2 equivalent over multiple months in Sodankylä, Finland**

3 David Brodylo¹, Lauren V. Bosche¹, Ryan R. Busby², Elias J. Deeb³, Thomas A. Douglas¹, Juha
4 Lemmetyinen⁴

5 ¹U.S. Army Cold Regions Research and Engineering Laboratory, Fort Wainwright, AK 99709, USA

6 ²U.S. Army Construction Engineering Research Laboratory, Champaign, IL 61826, USA

7 ³U.S. Army Cold Regions Research and Engineering Laboratory, Hanover, NH 03755, USA

8 ⁴Finnish Meteorological Institute, 00101 Helsinki, Finland

9 *Correspondence to:* David Brodylo (david.brodylo@usace.army.mil)

10 **Abstract.** Snowpack characteristics such as snow depth and snow water equivalent (SWE) are widely studied in regions prone
11 to heavy snowfall and long winters. These features are measured in the field via manual or automated observations and over
12 larger spatial scales with stand-alone remote sensing methods. However, individually these methods may struggle with
13 accurately assessing snow depth and SWE in local spatial scales of several square kilometers. One method for leveraging the
14 benefits of each individual dataset is to link field-based observations with high-resolution remote sensing imagery and then
15 employ machine learning techniques to estimate snow depth and SWE across a broader geographic region. Here, we combined
16 field-based repeat snow depth and SWE measurements over six instances from December 2022 to April 2023 in Sodankylä,
17 Finland with Light Detection and Ranging (LiDAR) and WorldView-2 (WV-2) data to estimate snow depth, SWE, and snow
18 density over a 10 km² local scale study area. This was achieved with an object-based machine learning ensemble approach by
19 first upscaling more numerous snow depth field data and then utilizing the estimated local scale snow depth to aid in estimating
20 SWE over the study area. Snow density was then calculated from snow depth and SWE estimates. Snow depth peaked in
21 March, SWE shortly after in early April, and snow density at the end of April. The ensemble-based approach had encouraging
22 success with upscaling snow depth and SWE. Associations were also identified with carbon- and mineral-based forest surface
23 soils, alongside dry and wet peatbogs.

24 **1 Introduction**

25 Seasonal snow is found in regions of the globe that experience freezing temperatures and is widely studied to monitor
26 changes in climate and hydrology. Snow is a component of the cryosphere that is heterogeneous over space and time. Snowmelt
27 provides drinking and irrigation water to approximately one sixth of the world's population (Barnett et al., 2005). The initial
28 layering of the snowpack is impacted by the deposition of falling snow, windblown snow redistribution, or a combination of
29 the two (Nienow and Campbell, 2011). Further densification can occur due to compaction and metamorphic mechanisms,
30 alongside meltwater, percolation, and refreeze events (Prowse and Owens, 1984; Tuttle and Jacobs, 2019; El Oufir et al., 2021;

31 Colliander et al., 2023). Given these factors, key elements of snow density are the age of the snowpack, snow depth, and water
32 content. Fresh snow can have a snow density of $0.05 - 0.07 \text{ g/cm}^3$ while fresh damp snow can range from $0.10 - 0.20 \text{ g/cm}^3$
33 (Musket, 2012). In contrast, the snow density of older dry snow is roughly $0.35 - 0.40 \text{ g/cm}^3$ and for older wet snow is up to
34 0.50 g/cm^3 (Seibert et al., 2015). Very wet snow and firn, which is snow that failed to melt in the previous summer and did not
35 turn into ice, can contain a snow density ranging from $0.40 - 0.80 \text{ g/cm}^3$ (Musket, 2012; Arenson et al., 2021). Within the
36 northern hemisphere, there is an immense variation in average snow density which ranges from $0.05 - 0.59 \text{ g/cm}^3$ with an
37 overall long-term average snow density of $0.25 \pm 0.07 \text{ g/cm}^3$ (Zhao et al., 2023).

38 Despite the attainability of snow density classification, there are significant complexities with generating the
39 estimated snow density alongside the related snow depth and snow water equivalent (SWE) over large areas and in challenging
40 environments such as thick forests and mountainous terrain. Snow depth is simply the total depth of snow on the ground while
41 SWE can be defined as the resulting depth of water produced from the complete melt of a mass of snow (Henkel et al., 2018).
42 The quantity of SWE is determined by the amount of snow accumulation alongside the amount of snow melt and sublimation
43 (Xu et al., 2019). Field-based SWE datasets are both spatially and temporally scarce and can be expensive and labor intensive
44 to acquire (Henkel et al., 2018; Fontrodona-Bach et al., 2023). In contrast, field-acquired snow depth measurements are more
45 common, and are both easier and faster to obtain, though their spatial extent is also limited and can be challenging to obtain in
46 difficult or remote areas (Collados-Lara et al., 2020; Tanniru and Ramsankaran, 2023). Automated stations can be utilized to
47 collect snow measurements, which are rapidly becoming more commonplace, such as accounting for over 80% of the snow
48 depth observing network north of 55° N in Canada (Brown et al., 2021). However, such stations may sometimes be primarily
49 intended for non-climatic purposes such as for avalanche warnings and thus not be verified nor corrected for climatic trends
50 (Salzmann et al., 2014).

51 Alternatives to field-based methods of snow observations are the use of airborne and spaceborne sensors to estimate
52 snow properties which have achieved great success in recent decades (Nagler and Rott, 2000; Kelly et al., 2003; Marti et al.,
53 2016; Cimoli et al., 2017; Tsai et al., 2019). Such sensors achieve large spatial coverage and the ability to clearly differentiate
54 between snow and non-snow features (Nolin, 2010; Raghubanshi et al., 2023). However, many commonly used spaceborne
55 sensors such as with the Landsat series, the Moderate Resolution Imaging Spectroradiometer (MODIS), the Advanced Very
56 High Resolution Radiometer (AVHRR), and the Advanced Microwave Scanning Radiometer (AMSR-E/AMSR2) have
57 limitations. These are either not capable of directly estimating snow depth or SWE, or, if able, have limited penetration or
58 contain very coarse resolutions that make local scale estimation unattainable, in addition to potential cloud cover contamination
59 (Rodell and Houser, 2004; Green et al., 2012; Lu et al., 2022; Stillinger et al., 2023). Repeat images captured via airborne
60 Light Detection and Ranging (LiDAR) can serve to successfully estimate changes in snow depth (Deems et al., 2013; King et
61 al., 2023); however the flights needed for these are costly, weather dependent, and require trained pilots and LiDAR specialists
62 (Jacobs et al., 2021; Yu et al., 2022). While issues are present in relying solely on remote sensing for snow depth and SWE
63 estimation, a blending of remote sensing imagery and field-based snow data can serve to significantly improve snow depth
64 and SWE estimations (Kongoli et al., 2019; Pulliainen et al., 2020; Cammalleri et al., 2022; Venäläinen et al., 2023).

In addition to this, the inclusion of machine learning can expand the potential to estimate snow depth and SWE over spatial and temporal scales. Machine learning techniques have been successfully applied to predict such features across Earth, including high altitude and high latitude environments (Jonas et al., 2009; Bair et al., 2018; King et al., 2020; Zhang et al., 2021; Shao et al., 2022; Hu et al., 2023). Commonly employed algorithms including Artificial Neural Network (ANN), K-Nearest Neighbor (KNN), Multiple Linear Regression (MLR), Random Forest (RF), and Support Vector Machine (SVM) have achieved success in snow depth, SWE, and snow-liquid ratio estimations (Broxton et al., 2019; Douglas and Zhang, 2021; Ntokas et al., 2021; Vafakhah et al., 2022; Hoopes et al., 2023; Liljestrand et al., 2024). Deep learning models such as Convolutional Neural Networks (CNNs) have also successfully been employed to estimate snow cover, snow depth, and SWE at various scales across the globe (Nijhawan et al., 2019; Xing et al., 2022; Duan et al., 2024; Kesikoglu, 2025). Individually many of these algorithms can produce positive results, though there may be a tendency for disagreement in model accuracy and outcomes (Li et al., 2023). As an alternative, a weighted ensemble-based empirical model can be utilized to potentially increase model accuracy, while also reducing estimation error (Douglas and Zhang, 2021; Brodylo et al., 2024). As each algorithm is optimized differently to generate outputs, each containing their pros and cons, an ensemble approach can improve feature estimation to ensure optimal results (Pes, 2020). A combination of such machine learning models, remote sensing imagery, and field-based snow data can thus provide the necessary foundations to map snow features across the cryosphere, which has been experiencing rising temperatures and increasing climatic uncertainty (Pan et al., 2017; Yang et al., 2020; Santi et al., 2022).

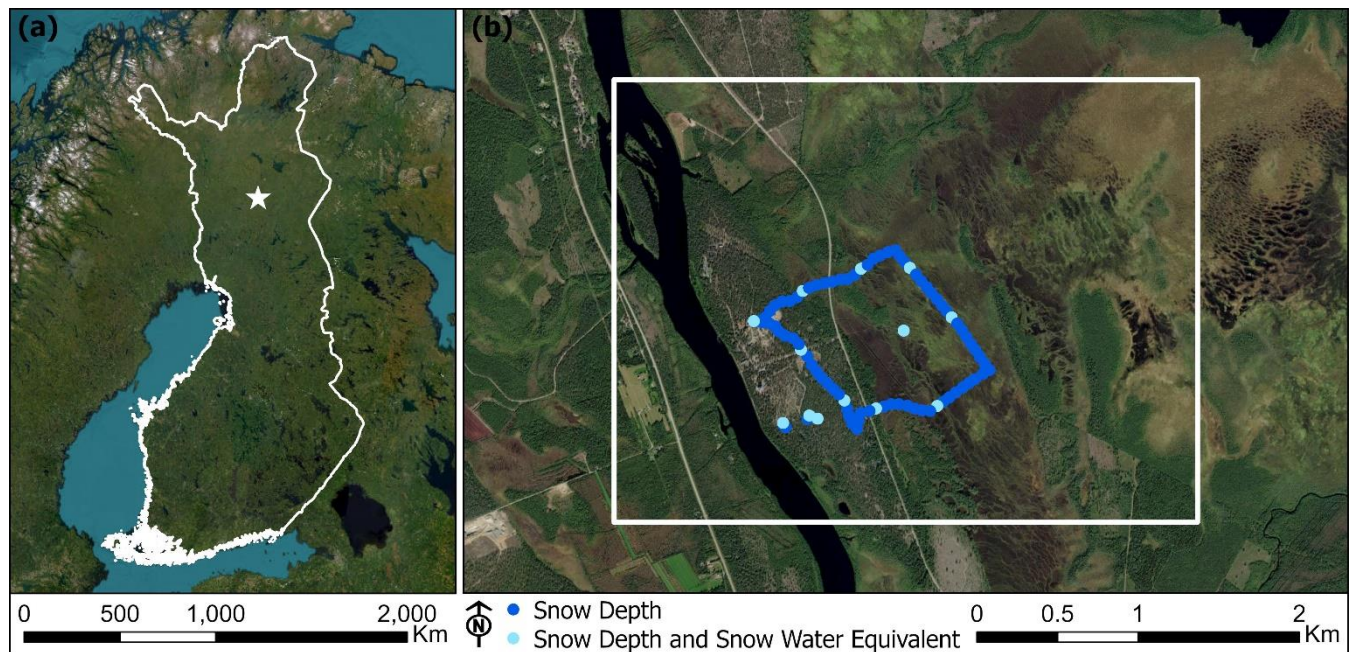
One region where application of such a technique is worthwhile is in northern Europe, particularly in the Lapland region located largely within the Arctic Circle. The area around Sodankylä, Finland is prone to long, cold winters with abundant snowfall and both on-the-ground snow depth and SWE measurements are available for multiple months or more. Here, we sought to utilize an object-based hybrid deep learning and machine learning ensemble approach with a combination of time-series field and automated snow data, alongside WorldView-2 (WV-2) imagery and LiDAR data to upscale snow depth, SWE, and snow density to a 10 km² local scale. This was implemented over six instances from December 2022 to April 2023, with snow estimates matched to dominant vegetative communities. Field-based snow depth observations were upscaled first, before utilizing the estimated snow depth to aid in upscaling more limited SWE field data to the local scale, with snow density then being mapped. Distinctive machine learning algorithms were employed and compared to an ensemble-based technique for both snow depth and SWE estimation.

2 Study area and data

2.1 Study area

The study area is found near the town of Sodankylä in the Sodankylä municipality of northern Finland, which is roughly 125 km north of the Arctic Circle. The 10 km² site is located along the Kitinen River and hosts the Finnish Meteorological Institute Arctic Space Centre (FMI-ARC) and the Sodankylä Geophysical Observatory (Bösinger, 2021)

97 between 67.356° N, 26.609° E, and 67.381° N, 26.693° E (Fig 1). It is largely flat, with elevations ranging between 170 and
98 190 m above sea level. Landcover consists primarily of coniferous and deciduous dominated forests and peat bogs, contains
99 organic and mineral soils, and portrays a standard flat northern boreal forest/taiga setting (Rautiainen et al., 2014). Field
100 analysis revealed a multitude of vegetative species at the study site. Dominant tree species are *Betula pubescens* (downy birch)
101 and *Pinus sylvestris* (Scots pine). Common shrub species include *Andromeda polifolia* (bog rosemary), *Empetrum nigrum*
102 (crowberry), *Rhododendron tomentosum* (Labrador tea), *Vaccinium cespitosum* (dwarf bilberry), *Vaccinium myrtillus*
103 (bilberry), *Vaccinium oxycoccus* (cranberry), and *Vaccinium vitis-idaea* (lingonberry). Graminoid species were comprised of
104 *Carex lasiocarpa* (woollyfruit sedge), *Danthonia decumbens* (heath grass), *Eriophorum vaginatum* (tussock cottongrass),
105 *Scheuchzeria palustris* (pod grass), and *Trichophorum cespitosum* (tufted bulrush). Forb species include *Comarum palustre*
106 (purple marshlock) and *Menyanthes trifoliata* (bog bean). Lichen and moss are also common.
107

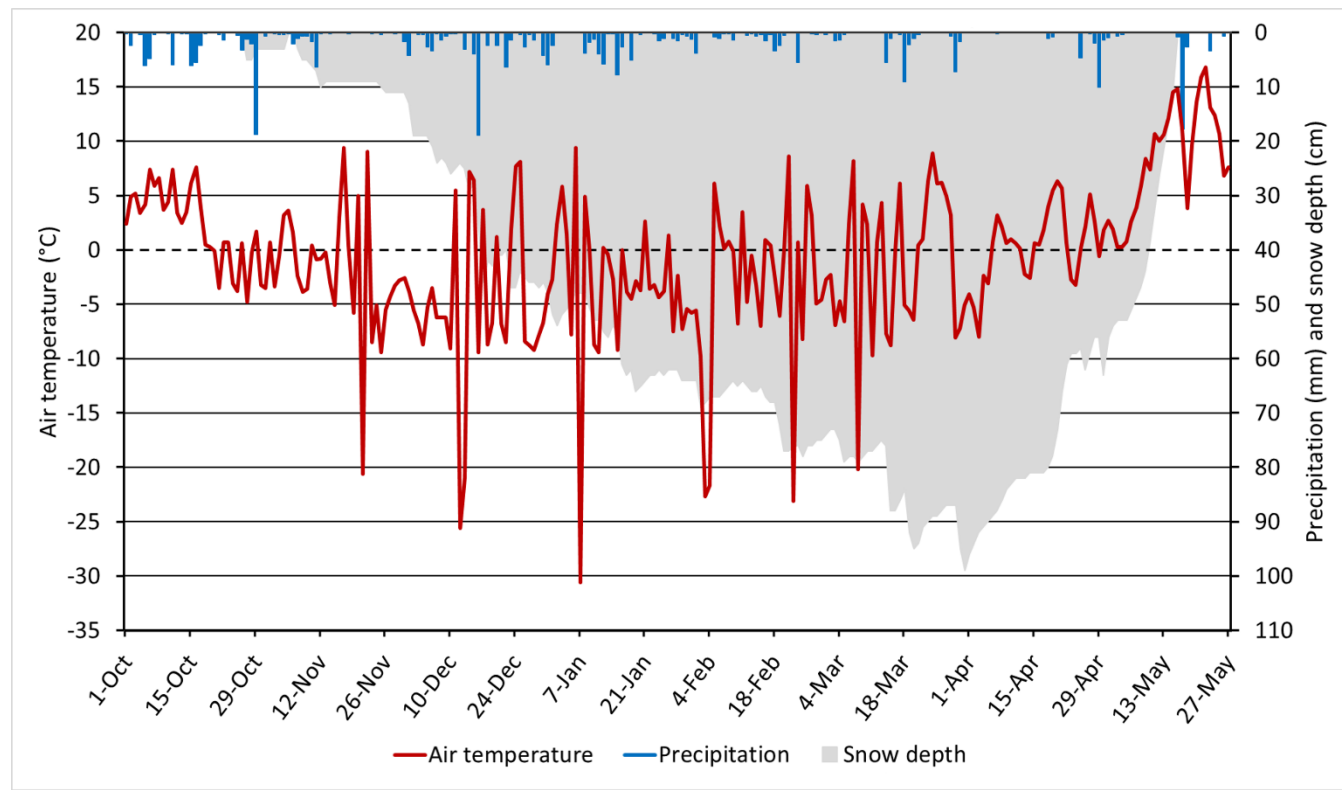


108
109 **Figure 1: Study area (a) in Sodankylä, Finland and (b) automated and manual snow depth and snow water equivalent measurements**
110 **within the 10 km² local scale study site. Image credits: © Esri, Earthstar Geographics, and Maxar.**

111
112 The climate in Sodankylä is defined by short but relatively warm summer season and a long and cold winter, with
113 snow present from October to May. Taiga snow is dominant, with thick layering of depth hoar at the base of the snowpack
114 (Anttila et al., 2014). Meaningful rain-on-snow events occur in November and early December (Bartsch et al., 2023). Between
115 1991 and 2020 at the FMI Sodankylä Tähtelä weather station, the average yearly precipitation was 543 mm with an average
116 yearly maximum snow depth of 91 cm that ranged from 65 – 127 cm. The average air temperature was 0.4 °C, the average
117 minimum was -4.2 °C, and the average maximum was 4.8 °C. The absolute minimum temperature was -49.5 °C while the

118 absolute maximum was 32.1 °C. The mean annual air temperature has increased by 0.07 °C from 2000 – 2018 (Bai et al.,
119 2021) and is expected to continue. Between the winters of 2007/08 to 2013/14 around FMI-ARC and the Sodankylä
120 Geophysical Observatory, the maximum SWE ranged approximately from 150 – 250 mm (Essery et al., 2016). For the winter
121 of 2022/23, a maximum snow depth of 99 cm was recorded at the Sodankylä Tähtelä weather station on 31 March 2023, with
122 rapid snow melt in April and early May (Fig 2). The average air temperature was generally near or below freezing in winter
123 and contained relatively low precipitation. The site generally contains low wind speeds that limit windblown snow
124 redistribution, with a monthly average of 2.5 – 2.9 m s⁻¹ above the forest canopy (Meinander et al., 2020).

125



127 **Figure 2: Daily average air temperature (°C), precipitation (mm), and snow depth (cm) from the FMI Sodankylä Tähtelä weather**
128 **station from 01 October 2022 – 27 May 2023.**

129 **2.2 Ground-based and remotely sensed measurements**

130 Field-based snow data were acquired over distinct vegetative communities on 14 December 2022, 17 January 2023,
131 15 February 2023, 17 March 2023, 17 April 2023, and 28 April 2023. Manually obtained snow depth was measured with a
132 fixed stake or manual probe, while SWE was calculated with a scale that is paired to a snow tube that is 70 cm high and 10 cm
133 in diameter that includes a scale on the outside to measure snow depth (Leppänen et al., 2016). Automated observations were
134 performed for snow depth with the Campbell Scientific SR50 sonic distance instrument and for SWE with the Sommer

135 Messtechnik SSG 1000 snow scale instrument. A total of 88 repeat snowpack depth (cm) measurements were taken at the
136 same locations with 80 being manually recorded and 8 being acquired from automated stations (Fig 1(b)). Of these same 88
137 locations, a total of 13 repeat SWE (mm) measurements were recorded: 11 manually and 2 from automated stations. SWE
138 values were based on the total snowpack depth. An average daily value was recorded from the automated stations to match
139 with the field-based observations, with previously strong correlations found between the automated and manual measurements
140 for both snow depth and SWE with average correlation coefficients of 0.98 and 0.99, respectively (Leppänen et al., 2018).
141 Snow density (g/cm^3) was calculated from dividing SWE by snow depth at the same location.

142 On-the-ground vegetation data were acquired between 31 July and 4 August 2023 from collaborative efforts by FMI
143 and the U.S. Army Corps of Engineers (USACE). Plots were established randomly along the snow depth measurement route
144 to encompass major plant community types, primarily coniferous and hardwood forests, and forested and herbaceous bogs. At
145 each plot, a center point was established, flags were placed in each cardinal direction to create a circular plot with a 7.3 m
146 radius, and GPS coordinates of the center point and flags were recorded. In each plot, all trees with diameter at breast height
147 (DBH) greater than 10 cm were recorded by species and DBH. Five 0.5 m^2 quadrats were randomly placed in each plot quadrant
148 and aerial cover of the understory vegetation was estimated in 5% increments for the following functional groups: moss, lichen,
149 shrub, forb, and graminoid.

150 Cloud free and high spatial resolution (2 m) spaceborne WV-2 images from MAXAR were acquired on 02 August
151 2021 and 27 April 2023. The summer imagery contained spectral readings that matched with distinct vegetative communities,
152 while the winter imagery served to identify snow and non-snow features. Snow-free LiDAR data from 2020 was gathered from
153 the National Land Survey of Finland (NLS) at a density of 5 pulses/ m^2 . Airborne LiDAR data were obtained on 27 April and
154 11 May 2023 by NV5 Geospatial and contained full to partial snow cover. This was captured with a Leica City Mapper-
155 2/Hypersion 2+ system containing an average pulse density of ≥ 25 pulses/ m^2 , absolute vertical accuracy of ≤ 6 cm, relative
156 vertical accuracy of ≤ 15 cm, and horizontal accuracy of ≤ 14 cm. The LiDAR data were further separated into a Digital Terrain
157 Model (DTM), Digital Surface Model (DSM), and Canopy Height Model (CHM). No major landcover changes impacted the
158 study site during these time periods that would have necessitated the need for repeat sets of imagery.

159 Land Use Land Cover (LULC) data were acquired from CORINE (Coordination of Information on the Environment)
160 Land Cover (CLC) at 20 m resolution from 2018. CLC is a LULC monitoring program that is coordinated by the European
161 Environment Agency (EEA) and is a current product of the Copernicus Land Monitoring Service (Aune-Lundberg and Strand,
162 2021). The LULC data was utilized to link vegetative communities to snow depth and SWE in the study area, while excluding
163 artificial features and water bodies. We downscaled the dataset to match the 2 m resolution WV-2 imagery and then updated
164 land cover boundaries where there were evident differences with the obtained summer imagery, thereby providing an updated,
165 higher-resolution LULC. In addition, a modified classification scheme was employed that sought to separate forest
166 communities by soil type and wetlands by moisture content. A RF-based classification scheme was employed for the final land
167 cover predictions and achieved an Overall Accuracy (OA) of 91.7% and a Kappa value of 0.91, which indicated high LULC
168 classification accuracy. A summary of gathered field and remote sensing variables can be seen in Table 1.

169

170 **Table 1: Summary of field and remote sensing variables.**

Data	Variables	Resolution	Source
Repeat Field Observations	Snow depth (cm) and SWE (mm)	In-situ	FMI
Field Vegetation Survey	Vegetative type and species	In-situ	USACE; FMI
WorldView-2	Multispectral bands	2 m	MAXAR
Snow-free LiDAR	DTM, DSM, CHM, and slope	5 pulses/m ²	NLS
Snow-on LiDAR	DTM, DSM, CHM, and slope	25 pulses/m ²	NV5 Geospatial
Land Use Land Cover	Land cover and vegetation	20 m	CORINE

171

172 **3 Methodology**173 **3.1 Image segmentation**

174 An Object-Based Image Analysis (OBIA) technique was utilized to make estimations of snow depth and SWE at the
 175 10 km² local site scale. In OBIA an image is separated into similar groupings of homogeneous pixels known as image objects
 176 or segments, which are then utilized as the spatial unit for image assessment (Ye et al., 2018). This contrasts with more
 177 traditional pixel-based classification methods, in which image assessment is performed on a pixel-by-pixel basis. The OBIA
 178 approach was selected as it has been found to deliver enhanced accuracy and results over traditional pixel-based approaches,
 179 especially with high-resolution imagery (Sibaruddin et al., 2018; Shayeganpour et al., 2021; Ez-zahouani et al., 2023).
 180 Additionally, outputs generated from traditional pixel-based approaches can be susceptible to high local spatial heterogeneity
 181 between adjacent pixels, commonly known as the “salt-and-pepper” effect, which is not evident with OBIA (Wang et al.,
 182 2020).

183 Image segmentation was accomplished with the Segment Mean Shift tool in ArcGIS Pro software, a desktop GIS
 184 application. It contains a nonparametric iterative technique that utilizes kernel density estimation to generate image objects
 185 from a maximum of three image bands by grouping nearby pixels that contain similar spectral characteristics (Goldberg et al.,
 186 2021). The red, green, and near-infrared bands were utilized from the summer WV-2 imagery to carry out image segmentation.
 187 For parameters, the spectral detail was set to 19 (near maximum) while spatial detail was set to 1 (minimum) to improve
 188 segmentation as both heterogeneous and homogenous areas were present. A total of 37,917 unique image objects were created.
 189 Mean and standard deviation were calculated for each image object from the LiDAR and WV-2 datasets. Additional indices
 190 utilized included the Green Chlorophyll Index (GCI), Red-Edge Chlorophyll Index (RECI), Normalized Difference Vegetation
 191 Index (NDVI), Normalized Difference Water Index (NDWI), and Soil-Adjusted Vegetation Index (SAVI). Descriptions of
 192 these widely utilized indices, beyond the scope of this work, are available in Gaitán et al. (2013), Xue and Su. (2017), and

193 Nadjla et al. (2022). The automated and field-based snow depth and SWE measurements were spatially joined to polygons
194 with a 3 m radius at each observed field point that each contained average and standard deviation raster band values. This was
195 done to ensure that the input data in this approach better incorporated the spatial context of surrounding features and to improve
196 modeling performance.

197 **3.2 Machine learning models**

198 In addition to a deep learning Convolutional Neural Network (CNN), other commonly utilized and unique supervised
199 regression-based machine learning models entailing of Random Forest (RF), Support Vector Machine (SVM), Artificial Neural
200 Network (ANN), and Multiple Linear Regression (MLR) were chosen to estimate snow depth and SWE for the image objects.
201 RF works by training a large collection of decision trees to generate an optimal output via bootstrap aggregation (Hwang et
202 al., 2023). In contrast, SVM is a supervised algorithm that relies on an optimal hyperplane that minimizes error bounds and
203 seeks to identify a function that best predicts a continuous output value (Pimentel et al., 2021). ANN may be explained as a
204 feed-forward Directed Acyclic Graph (DAG) connected with artificial neurons with nonlinear activation functions (Li et al.,
205 2022). The architecture of the ANN model used in this manuscript was a feed-forward model with a single hidden layer. MLR
206 models the linear relationship between independent variables to a dependent variable by finding the best-fitting linear equation.
207 (Kim et al., 2020). CNN is an ANN model that includes at least one convolutional layer (Santry, 2023), though often contains
208 some combination of convolutional layers, pooling layers, and dense layers. The tuneGrid parameter found in the caret package
209 in R was used to specify a grid of hyperparameter values for tuning the model training process to optimize machine learning
210 performance. Further details on the hyperparameter values can be found in Appendix A. To aid in reducing potential modeling
211 bias and overfitting, a k -fold cross-validation technique was employed. With this, matched data samples are randomly split
212 into k number of subsets, with $k-1$ being utilized to train models and the remainder to test models (Abriha et al., 2023). Here,
213 a k -fold of 10 was utilized whereby in each subset 90% of the data is assigned for training and 10% is for testing, with output
214 metrics determined from the average of all iterations. Thus, each subset of randomly split data is utilized for testing only once,
215 before rejoining the training set. For preprocessing, all inputs were standardized, and a Principal Component Analysis (PCA)
216 was utilized prior to running each model, which also aided to lessen model overfitting.

217 **3.3 Object-based ensemble machine learning**

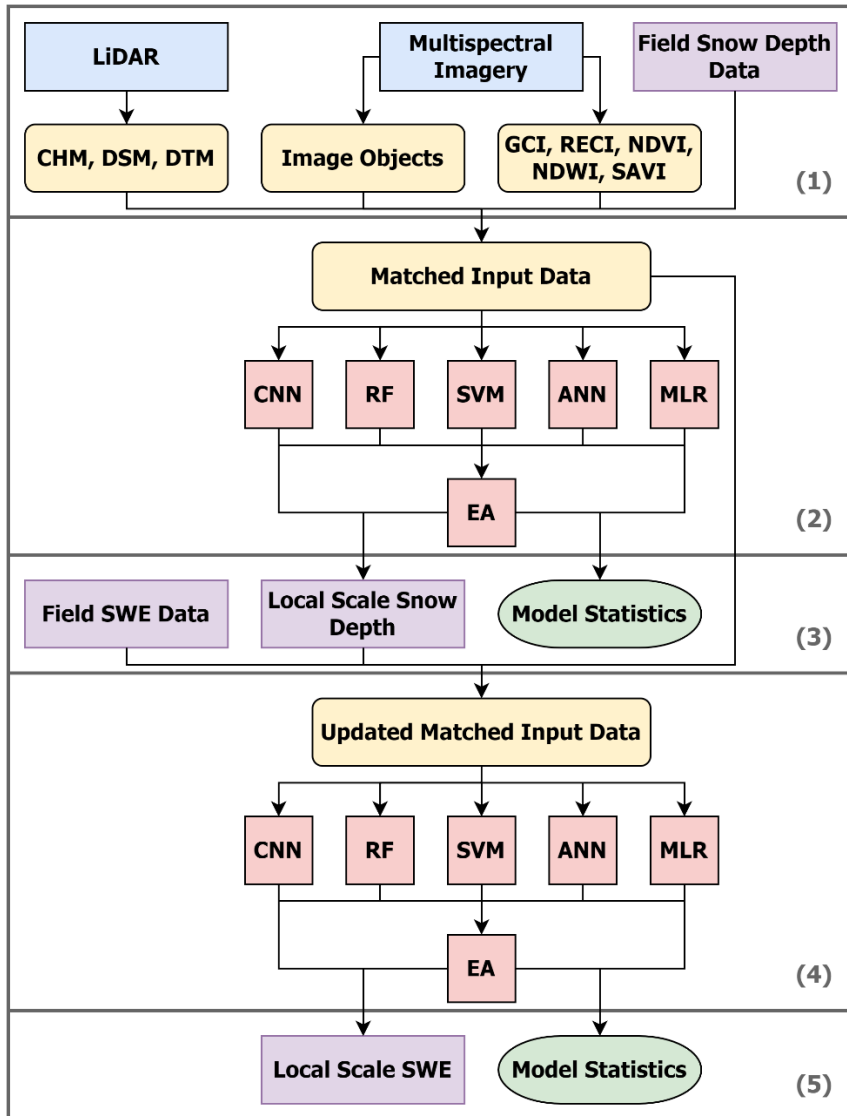
218 An object-based hybrid deep learning and machine learning ensemble approach was applied from a combined
219 weighted output of the CNN, RF, SVM, ANN, and MLR models which is referred to here as Ensemble Analysis (EA). Given
220 that these individual models compute predictions differently and will have varying accuracies and errors, EA can result in a
221 more robust model that considers more accurate models while minimizing the influence of less accurate ones. This is relevant
222 for repeat predictions over the same study site as a model may perform well in one scenario while underperforming in another,
223 such as with estimating snow depth during a period of low or high snowfall. All five models were included to estimate snow
224 depth and SWE. The model weights for EA were determined by the coefficient of determination (R^2) in which a model with a

225 larger R^2 value would be given a higher weight, and the sum of weights equal to 1.0 (Zhang et al., 2020). For EA, the weighted
226 average value for each predicted output were calculated by:

227
$$\bar{x} = \frac{(x_1 \cdot w_1) + (x_2 \cdot w_2) + \dots + (x_n \cdot w_n)}{w_1 + w_2 + \dots + w_n} \quad (1)$$

228 Where \bar{x} is the weighted average, n is the n^{th} machine learning model, x is the predicted snow depth or SWE value,
229 and w is the weighted model R^2 value. Combined model uncertainty for EA predictions was based on the standard deviation
230 of model outputs and is referred to as the standard deviation to ensemble prediction (STDE). Other statistical metrics included
231 the Mean Absolute Error (MAE), which is the absolute error between the observed and predicted values, and the Root Mean
232 Square Error (RMSE), which is more sensitive to outliers and is the square root of the mean squared error between observed
233 and predicted values. Larger differences between MAE and RMSE would serve to indicate a high variance of the individual
234 errors from the test samples. Local scale estimations were generated for snow depth via the ensemble-based approach, which
235 were then utilized as added inputs to aid in upscaling the more limited field acquired SWE data to the same local scale. Snow
236 density was measured by dividing the estimated SWE by the estimated snow depth in each respective instance. A summary of
237 the methodology framework can be found in Fig 3. Image objects were generated from multispectral imagery via image
238 segmentation, with averaged remote sensing and field snow depth values assigned to each unique image object (1). The
239 spatially matched data was then evaluated through the base machine learning models (CNN, RF, SVM, ANN, and MLR) to
240 predict snow depth before being ascertained with EA by combining model outputs with weighted averaging based on the R^2
241 value of each model (2). Model metrics were obtained from each model alongside the mapped estimated local scale snow
242 depth, with the estimated snow depth from EA and field SWE values then being spatially joined to the previously matched
243 input data (3). The updated spatially matched data was analyzed by the same base machine learning models (CNN, RF, SVM,
244 ANN, and MLR) to predict SWE before being finalized with EA (4). Model metrics were generated along with the mapped
245 estimated local scale SWE in each instance (5).

246



247

248 **Figure 3: Methodology framework to upscale field snow depth data to a local scale by using an object-based ensemble machine**
 249 **learning approach, and then joining the produced snow depth outputs and matched input data with the field SWE data to generate**
 250 **local scale SWE outputs. Blue indicates input data, purple indicates outcome variables, yellow indicates processed data, red**
 251 **indicates machine learning, and green indicates model metrics. RF is Random Forest, SVM is Support Vector Machine, ANN is Artificial**
 252 **Neural Network, MLR is Multiple Linear Regression, and EA is Ensemble Analysis.**

253 While the methodology is similar to that found in Brodylo et al. (2024), that work was solely intent on upscaling 1
 254 m^2 permafrost active layer thickness (ALT) field data to three 1 km^2 local scale sites in Alaska before then further upscaling
 255 the ALT estimates to a 100 km^2 regional scale over multiple years. Here, we focused on first upscaling repeat field snow depth
 256 measurements to a 10 km^2 local scale in Finland over multiple instances with a novel object-based hybrid deep learning and
 257 machine learning ensemble approach and then combined the estimated snow depth data to the original machine learning input
 258 data. The addition of snow depth as an input variable enabled a separate, enhanced estimate of SWE at the same 10 km^2 local

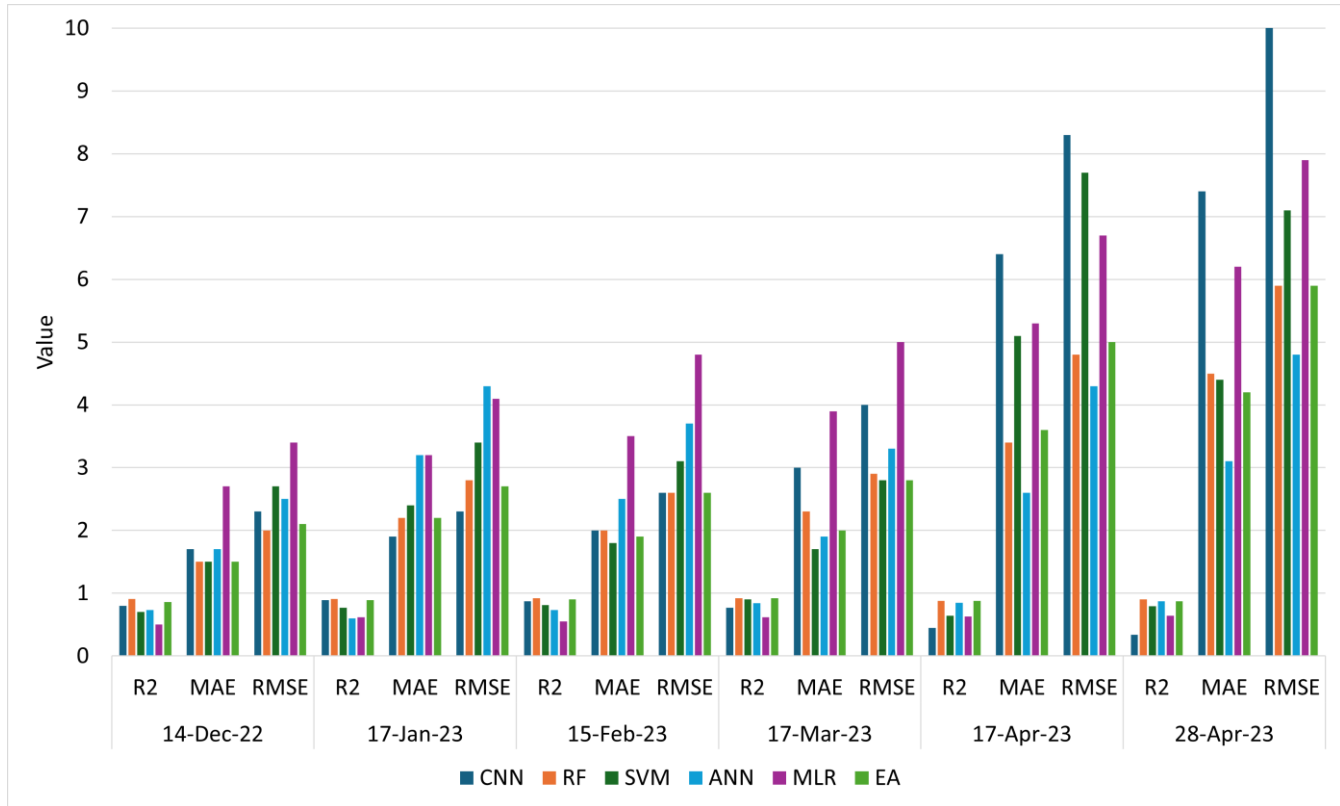
259 scale with more limited repeat field SWE measurements over the same multiple instances in a single winter period. This then
260 permitted snow density to be calculated at each moment in time from snow depth and SWE estimations. The approach was
261 applied to a shorter temporal analysis for snow depth, SWE, and snow density. It revealed how each of these variables were
262 interconnected during the initial, middle, and late winter, how machine learning models performed over the course of the
263 winter period, and how the studied variables related to landcover types over these different instances. In addition, machine
264 learning snow depth estimates were directly compared to independent LiDAR-based snow depth estimation.

265 **4 Results**

266 **4.1 Snow depth**

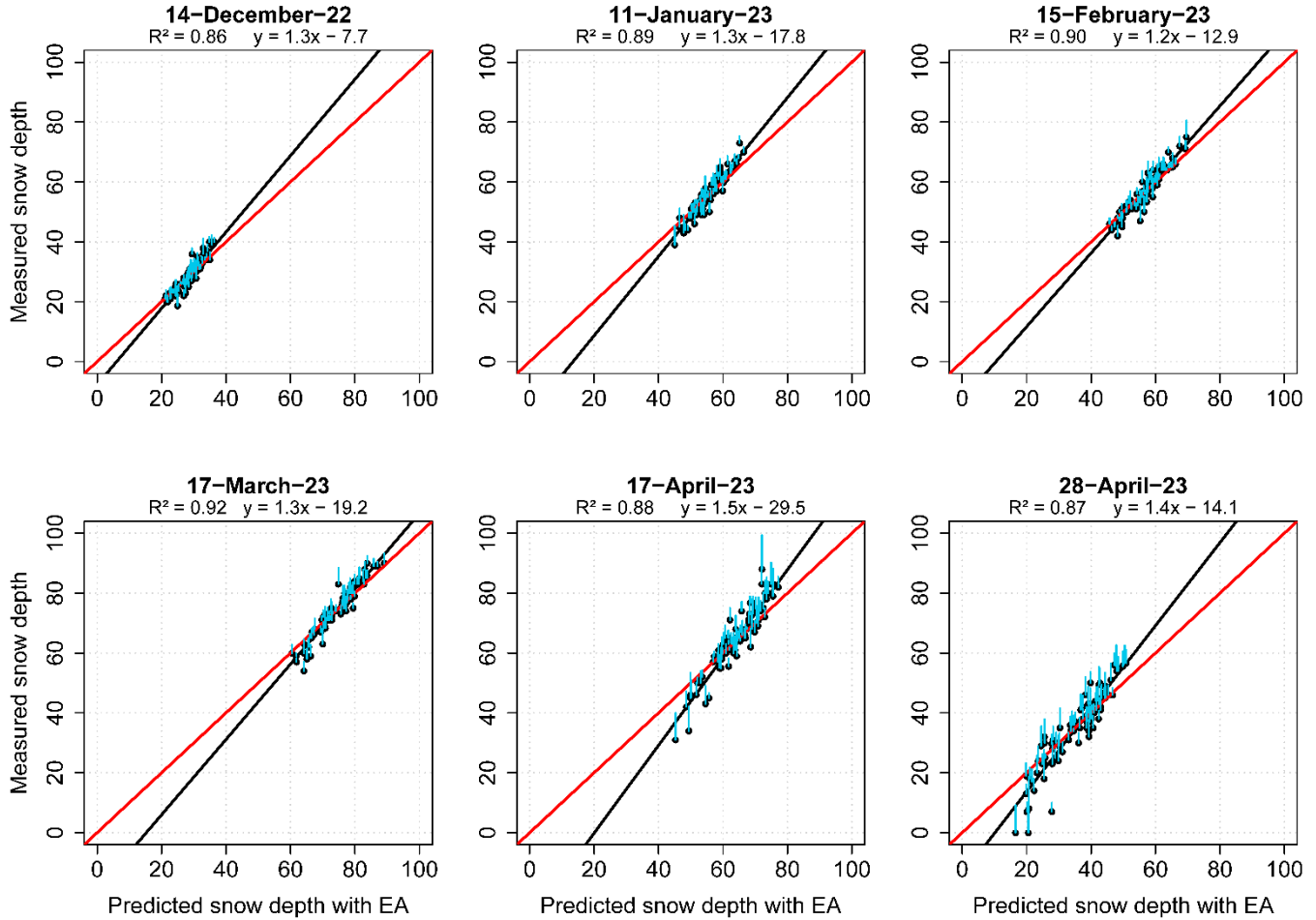
267 All tested models performed relatively well with the snow depth estimations. The best R^2 , MAE, and RMSE values
268 were observed with CNN, RF, SVM, ANN, and EA (Fig 4). Owing to the lower snow depth in December, MAE and RMSE
269 were the smallest out of all six instances at 1.5 cm and 2.1 cm for EA, respectively. MAE and RMSE steadily increased for all
270 models from roughly 1.5 – 2.7 cm and 2.0 – 3.4 cm in December to 3.1 – 7.4 cm and 4.8 – 10.0 cm at the end of April. This
271 was expected given increased snowfall and snow depth over time, alongside minor periods of snowmelt throughout and
272 accelerated snowmelt in April that would increase model uncertainty. The R^2 value for EA was strongest during peak snow
273 depth in March (0.92), while being somewhat lowered in December (0.86) during the lowest observed snow depth and late
274 April (0.87) during rapid snow melt. RF and EA tended to have the most consistent and best or second best R^2 , MAE, and
275 RMSE values across all six instances. This was in contrast with metrics produced from CNN, ANN, and MLR. CNN contained
276 metrics that were relatively in-line or better than other models between the first and fourth instance. However, in both instances
277 in April during the period of snowmelt there was a noticeable drop in metric performance. ANN and MLR were almost the
278 opposite, with having poorer performance in the beginning instances before notably improving performance from March to
279 the end of April when snow depth peaked and rapid snow melt was occurring. This improvement led to ANN producing some
280 of the best or second best metrics during that period, while MLR was still lagging in metric performance to most models. More
281 information about outputs produced with EA for each instance can be seen in Fig 5, with each instance containing a 1:1 line,
282 fitted linear regression line, and scatterplot with STDE error bars in blue. With minor exceptions, there was largely an overall
283 agreement between the field and estimated snow depth values, and between the individual model outputs.

284



285
286 **Figure 4: Machine learning model metrics for estimated snow depth with CNN, RF, SVM, ANN, MLR, and EA. MAE and RMSE**
287 **are in cm.**

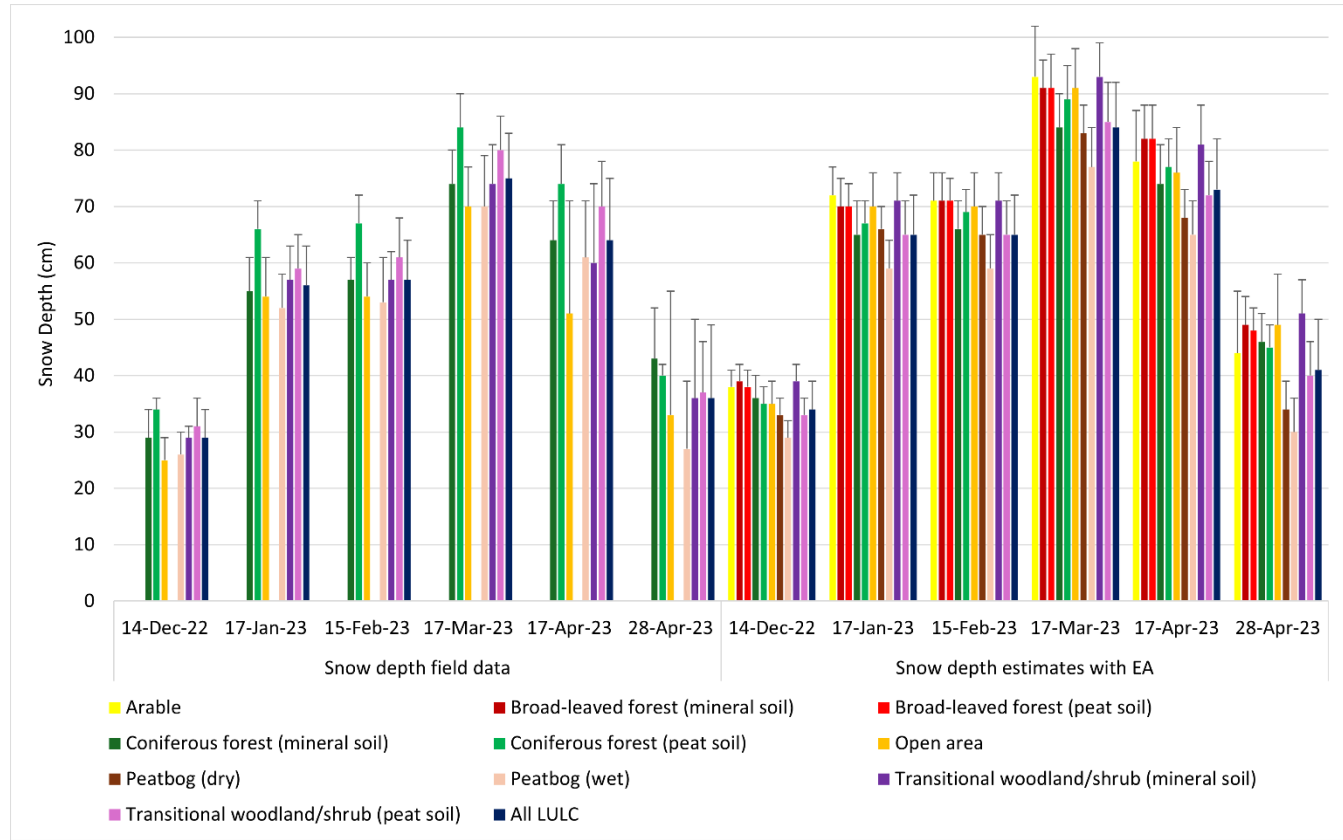
288

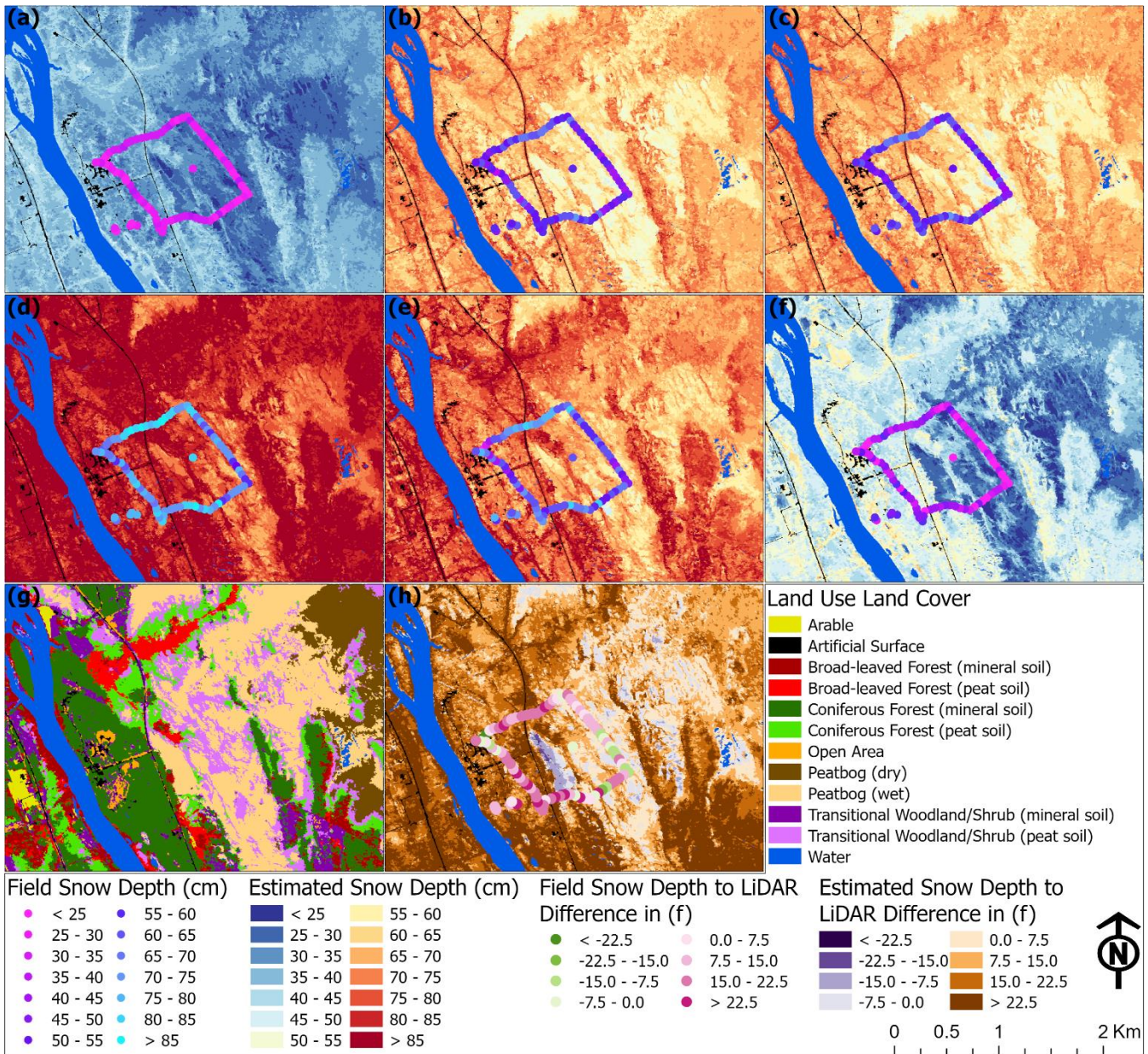


289
290
291 **Figure 5: Scatterplot, 1:1 line (red line), and fitted regression line (black line) between the predicted snow depth from EA and the
292 measured snow depth on each occasion from 14-December-2022 until 28-April-2023. STDE is in cyan.**

293
294 The snow depth average and standard deviation at each of the vegetative land cover types with the field data and local
295 scale EA outputs are in Fig 6. Mapped snow depth at the field scale and local scale estimates with EA for each instance from
296 December 2022 – April 2023 can be seen in Fig 7. There was a general agreement and similar snow depth patterns in LULC's
297 that contained both field and local scale data. The average snow depth was lowest for the field data at 29 cm and local scale at
298 34 cm in December, while the highest readings were in March at 75 and 84 cm, with a rapid decline at the end of April at 36
299 and 41 cm. Standard deviation was lowest in December at ± 5 cm for both while highest at the end of April (± 13 and ± 9 cm)
300 when there was increased snowmelt. At the field scale there was up to a 10 – 11 cm difference between coniferous forest (peat
301 soil) and coniferous forest (mineral soil) from January to early April. The exception is at the end of April during the period of
302 snowmelt when field coniferous forest (mineral soil) contained higher snow depth at 43 cm than coniferous forest (peat soil)

303 at 40 cm. A similar pattern was evident with the field transitional woodland/shrub (peat soil) repeatedly containing higher
 304 snow depths than transitional woodland/shrub (mineral soil) with a maximum difference of 10 cm in early April. However, at
 305 the end of April both were equal at 36 cm of snow depth. Field-based peatbog (wet) and open area contained the lowest levels
 306 of snow depth in all instances, ranging from 26 – 70 cm and 25 – 70 cm, respectively, with the latter experiencing elevated
 307 standard deviation of ± 20 and ± 22 cm in the last two instances.





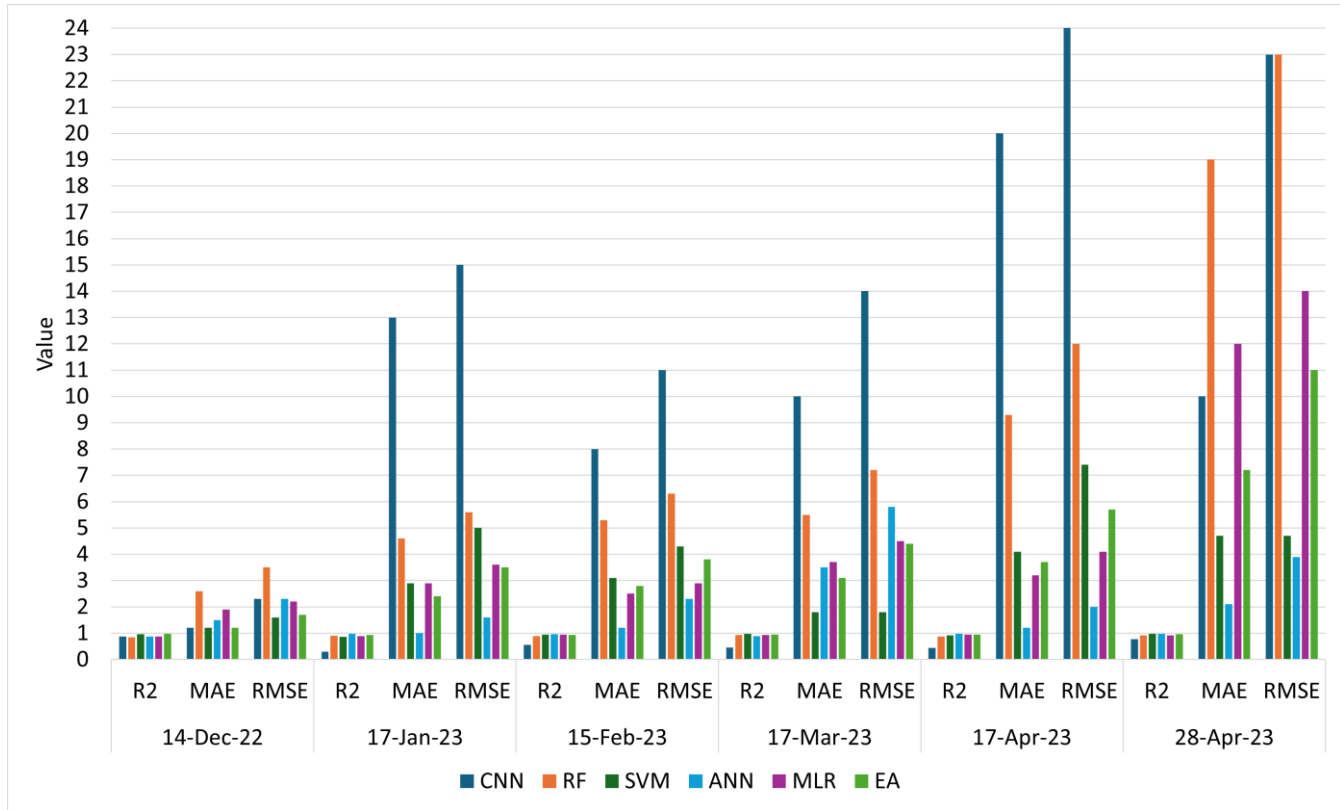
312
313 **Figure 7: Field and estimated snow depth (cm) in a 14-December-22, b 17-January-23, c 15-February-23, d 17-March-23, e 17-
314 April-23, and f 28-April-23 alongside g a LULC map and h 28-April-23 snow depth difference from 27-April-23 collected LiDAR.**

315
316 At peak snow depth at the local scale in March, both dry and wet peatbogs contained the lowest average snow depth
317 at 83 and 77 cm, alongside having the lowest snow depths in all other instances, particularly for wet peatbogs. Dry, unsaturated
318 peatbog was found to have snow depths greater than wet, saturated peatbog, with differences ranging from 3 cm to 7 cm.

319 Arable and open area contained similar estimated snow depth values in all instances except in the end of April with a 5 cm
320 difference and were higher than dry and wet peatbogs from January to the end of April. Forests and transitional woodlands
321 largely contained the higher average values in March with broad-leaved forest recording 91 cm (mineral soil) and 91 cm (peat
322 soil), coniferous forest (peat soil) with 89 cm, and transitional woodland/shrub containing 93 cm (mineral soil). There was also
323 a consistent 0-1 cm snow depth difference between the local scale broad-leaved forest peat soils and mineral soils. Transitional
324 woodland/shrub contained higher snow depth in mineral soil than in peat soil in all instances despite the field data having the
325 opposite pattern, which may be due to certain terrain and vegetative factors being higher prioritized in model performance for
326 areas further away from gathered field observations. Local scale coniferous forest (peat soil) consistently contained snow depth
327 values greater than coniferous forest (mineral soil), with up to a 5 cm difference from January to early April. The inverse
328 occurred with the mineral soil containing higher snow depth at the end of April for both the field and local scale data. In
329 addition, field and local scale snow depth estimates from 28 April were compared to the difference between snow covered
330 DTM from the prior day and snow-free DTM from 2020. Results indicate field snow depth measurements generally exceeded
331 the estimated LiDAR-based snow depth estimations by an average of 9.6 cm, while for the local scale with EA it was higher
332 at 16.7 cm.

333 **4.2 Snow water equivalent**

334 Machine learning model performance for SWE estimation between CNN, RF, SVM, ANN, MLR, and EA can be
335 seen in Fig 8. Given more limited field-based SWE measurements with 13 samples, the models would have encountered more
336 pronounced challenges matching estimations to real-world data yet were generally able to produce acceptable results in part
337 due to the inclusion of snow depth data. EA contained the most stable and positive metrics for R^2 in all instances. SVM, ANN,
338 and EA generally produced the best metrics, although MLR was able to provide the second-best metrics in some instances.
339 Metrics from CNN and to a lesser extent RF varied considerably, being on-par with the other models in December, though
340 CNN had poor performance between January and early April, while RF would consistently contain the second worst MAE and
341 RMSE values in the same period, while having the worst R^2 , MAE, and RMSE in December and the worst MAE and RMSE
342 at the end of April. While the best base model performance for EA inputs were CNN, RF, SVM, and ANN over different
343 instances for snow depth, for SWE it was largely from SVM, ANN, and to a lesser extent MLR in different instances. In both
344 cases, EA was able to provide positive metrics and was never poor metrics. A scatterplot, 1:1 line, and fitted linear regression
345 line for each instance of SWE predictions produced by EA alongside STDE can be seen in Fig 9. Similarly with the snow
346 depth metrics over the same period, MAE and RMSE were lowest in December from roughly 1.2 – 2.6 mm and 1.6 – 3.5 mm
347 before rising to become the highest at the end of April at 2.1 – 19.0 mm and 3.9 – 23.0 mm.



348 **Figure 8: Machine learning model metrics for estimated snow water equivalent with RF, ANN, MLR, and EA. MAE and RMSE are**
 349 **350 in mm.**

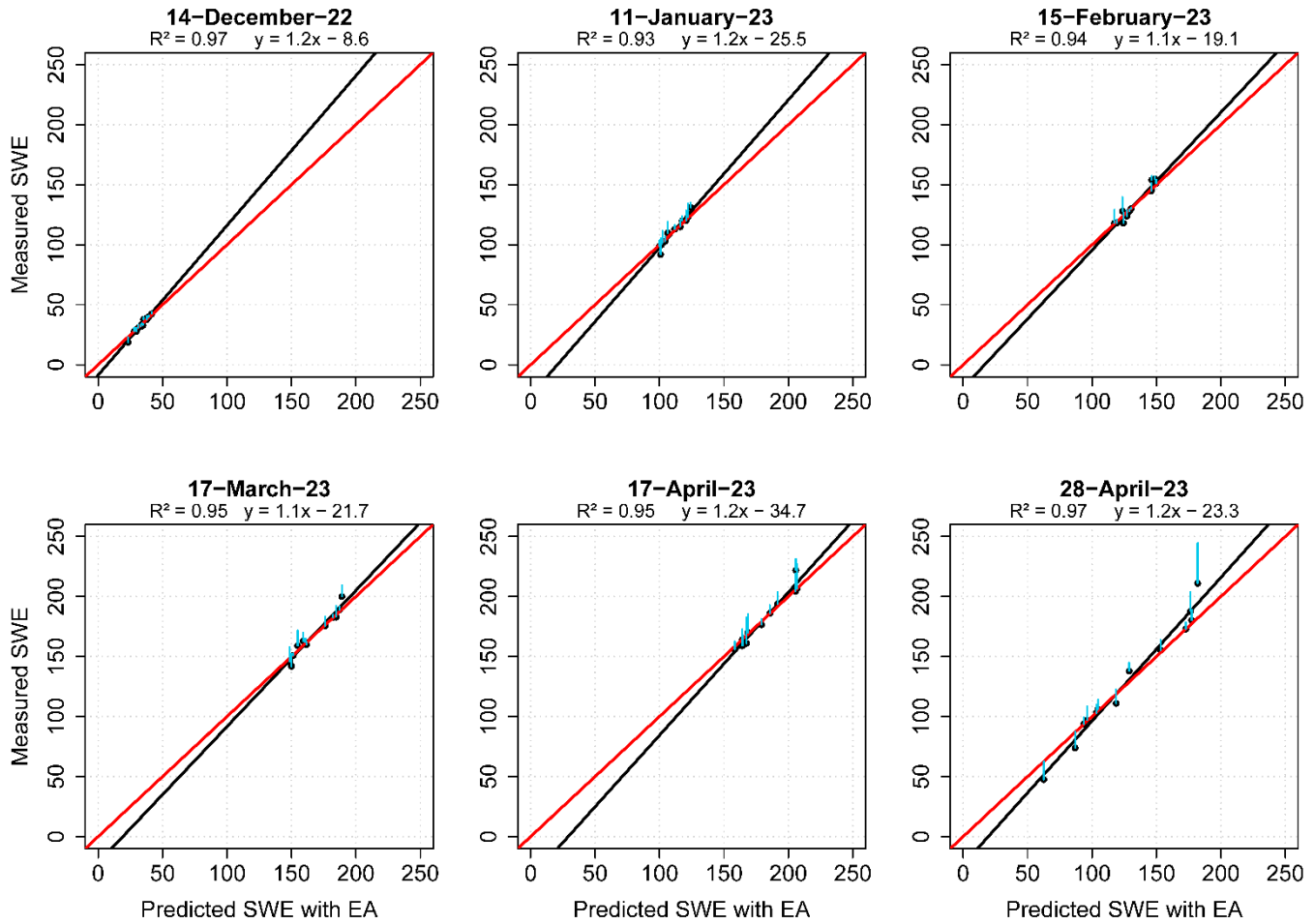
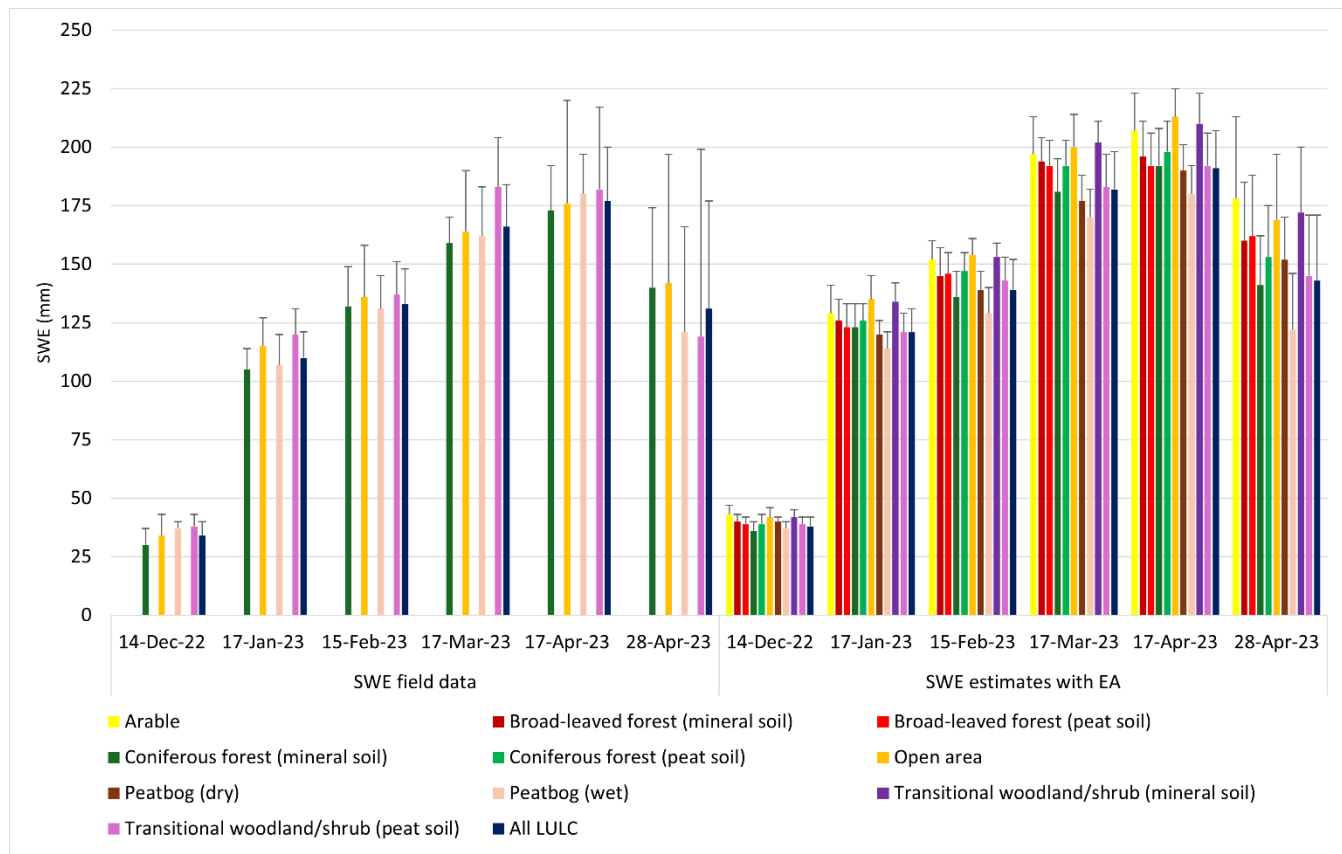
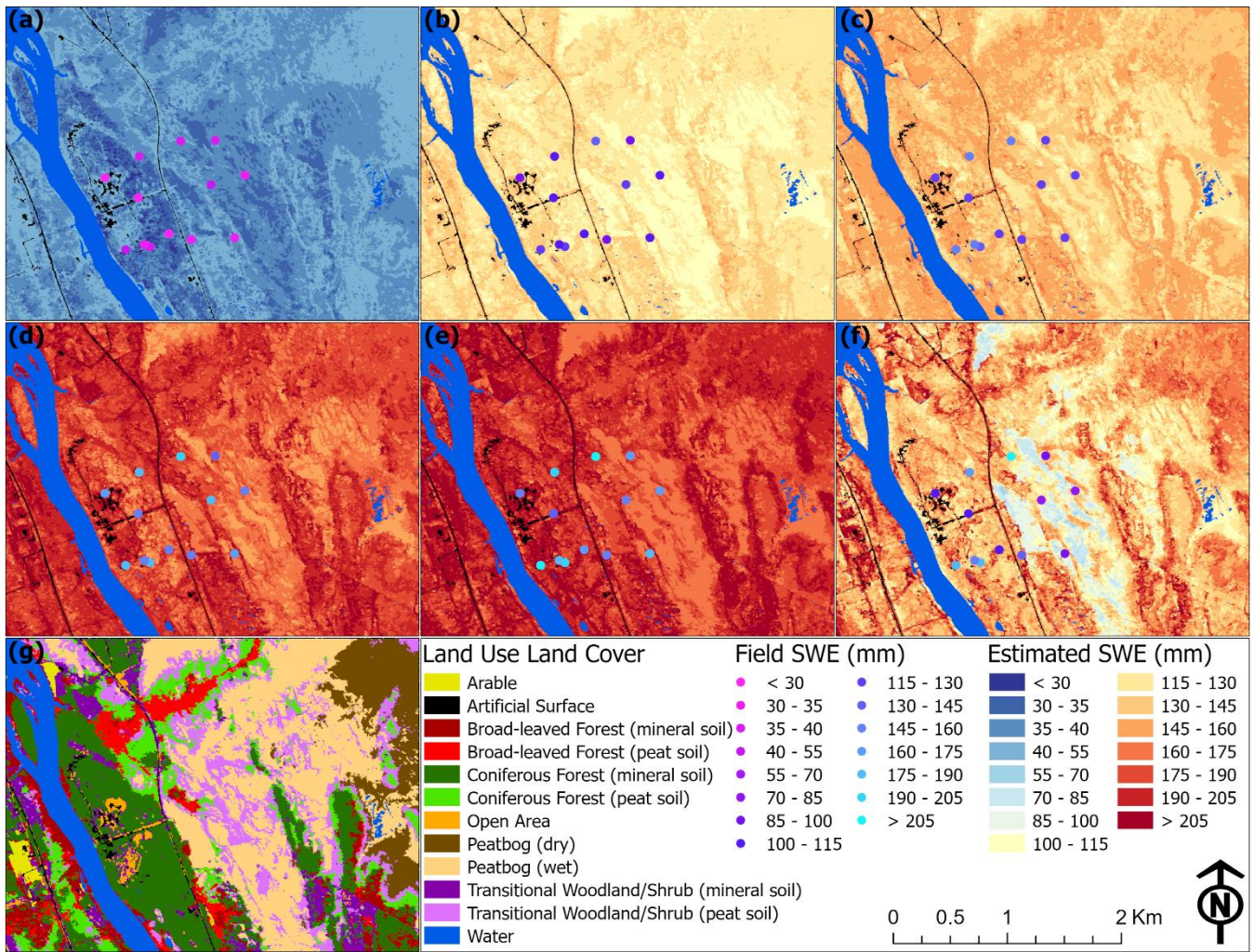


Figure 9: Scatterplot, 1:1 line (red line), and fitted regression line (black line) between the predicted SWE from EA and the measured SWE on each occasion from 14-December-2022 until 28-April-2023. STDE is in cyan.

The average and standard deviation of SWE field data and local scale EA outputs at the vegetative land cover types for all instances can be seen in Fig 10. A distribution of SWE over the 10 km² site for each instance from December 2022 – April 2023 can be seen in Fig 11, which illustrates where and how much SWE varied over time for the field data and EA-based local scale outputs. SWE maximums occurred in early April and were after peak snow depth in March. With the field data, the average SWE was lowest at 34 mm in December and then peaking at 177 mm in early April before dropping to 131 mm in late April. A similar pattern was evident with the local scale average SWE outputs with 38 mm in December that later peaked at 191 mm in early April before dropping to 143 mm at the end of April. From the field data, coniferous forest (mineral soil) largely had the lowest SWE values from December (30 mm) to early April (173 mm). This was in sharp contrast to transitional woodland/shrub (peat soil) which had the highest SWE values during that same period from 38 mm to 183 mm before dropping sharply to 119 mm at the end of April. Open area tended to have higher SWE values, while peatbog (wet) gravitated to lower

366 SWE values. Largely corresponding to the SWE quantity and time, standard deviation was lowest in December ranging from
367 ± 3 to ± 9 mm while highest at the end of April between ± 34 to ± 80 mm.
368





373
374 **Figure 11: Field and estimated SWE (mm) in a) 14-December-22, b) 17-January-23, c) 15-February-23, d) 17-March-23, e) 17-April-**

375 23, and f) 28-April-23 alongside g) a LULC map.

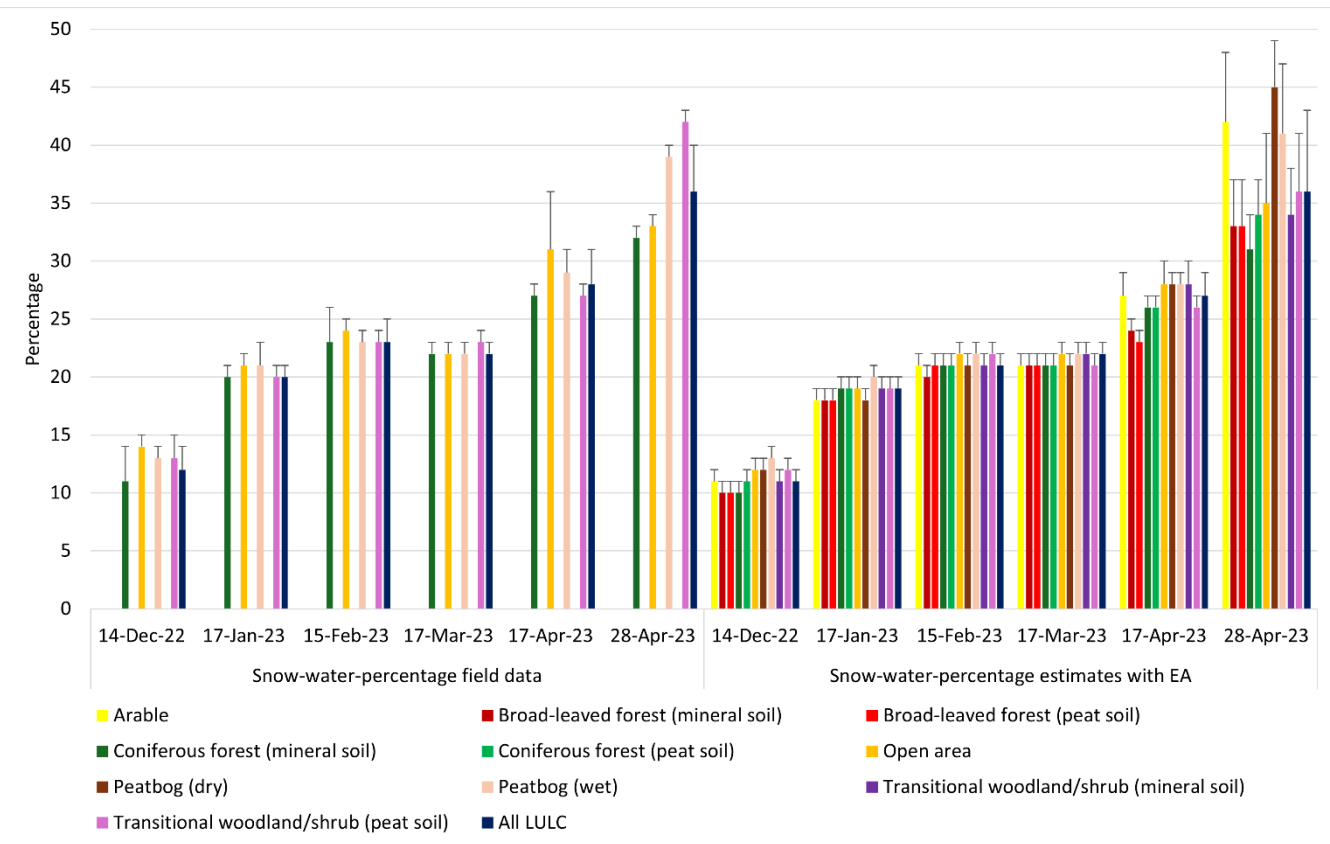
376 At the local scale, the landcover types with the highest SWE values in all instances were arable, open area, and
377 transitional woodland/shrub (mineral soil). These areas were similar in that they contained little to no inundated land along
378 with a lack of bushes and trees. The highest SWE values were in early April for all three landcover types at 207 mm, 213 mm,
379 and 210 mm respectively. The lowest SWE values in all instances tended to be found in coniferous forest (mineral soil),
380 peatbog (dry), peatbog (wet), and transitional woodland/shrub (peat soil). Peatbog (wet) contained the lowest SWE values
381 from January (114 mm) to the end of April (122 mm), which was somewhat in contrast to peatbog (dry) during the same period
382 from 120 mm in January to 152 mm at the end of April. SWE values for broad-leaved forest in mineral and peat soil tended
383 to be similar and slightly above average, while there was greater variation for coniferous forest. Coniferous forest (mineral soil)
384 consistently contained lower SWE values than did coniferous forest (peat soil) with differences between 3 to 12 mm.

385 Transitional woodland/shrub (mineral soil) also repeatedly had higher SWE values than transitional woodland/shrub (peat soil)
386 in all instances, with differences varying from 3 to 27 mm. The standard deviation values for the EA values were less volatile
387 than with the field data, with it ranging from 2 mm in December to 35 mm at the end of April.

388 **4.3 Snow density**

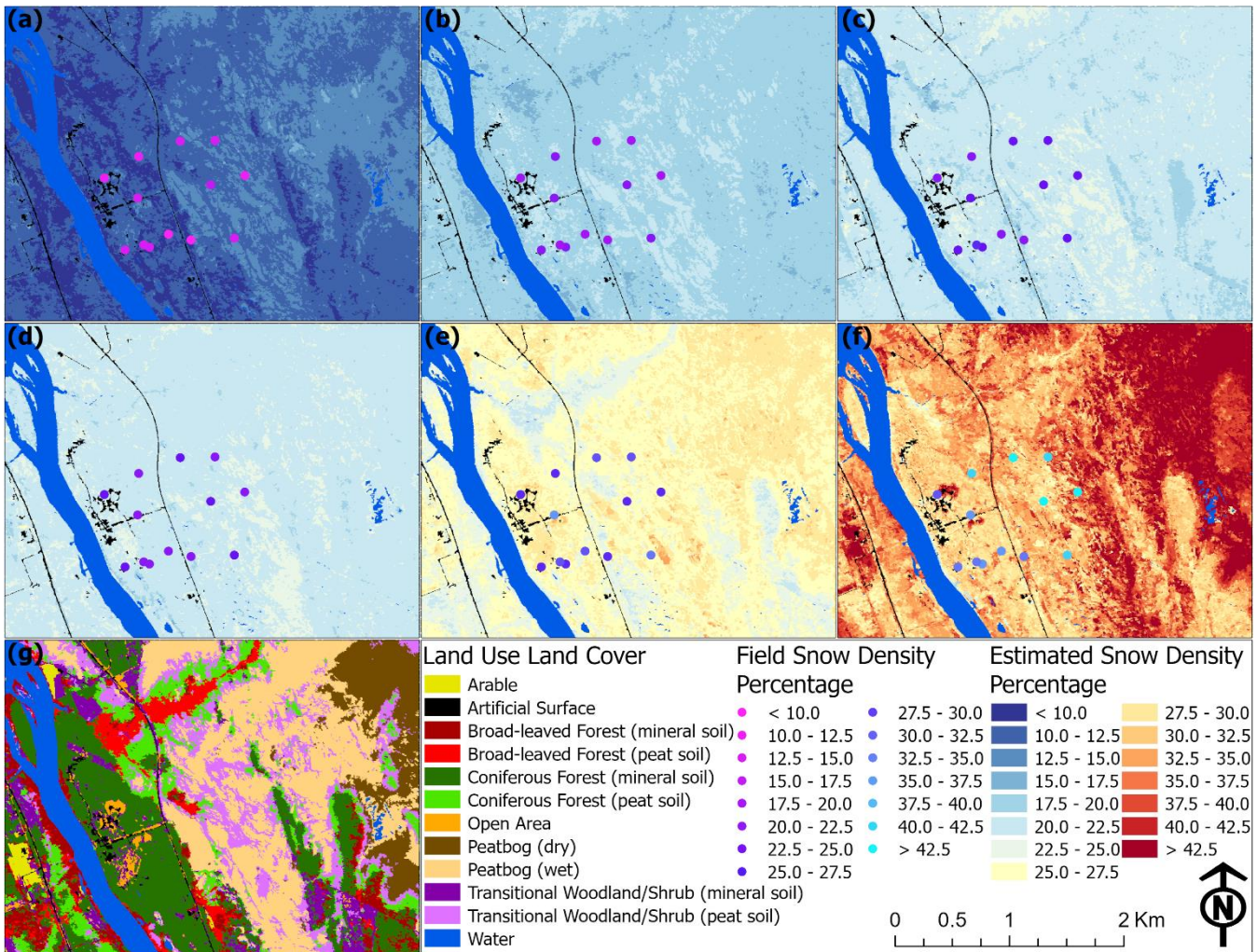
389 Snow density is the ratio between the volume of water produced by melting a given volume of snow and the original
390 volume of snow itself. This percentage refers to the water content within a given volume of snow. In general, fresh snowfall
391 has low density while older, compacted, or wind-effected snow will have a higher density. Fig 12 contains the mean and
392 standard deviation of the snow density percentage for each vegetative landcover type from December to the end of April. The
393 average snow density percentage for field and local scale data was lowest in December with 12% and 11%, respectively, while
394 the highest was at the end of April at 36% for both. Standard deviation for the combined averages were generally low, with a
395 maximum of $\pm 4\%$ and $\pm 7\%$ in late April for field and local scale EA estimates. While the field standard deviation for specific
396 landcover types could increase to $\pm 3\%$ prior to early April, for the local scale EA estimates it never reached $\pm 2\%$ during that
397 same period. For the first five instances the field snow density percentages were slightly higher with the canopy-free open area
398 and peatbog (wet), which ranged from 14 – 31% and 13 – 29%. In contrast, the more tree-covered coniferous forest (mineral
399 soil) and transitional woodland/shrub (peat soil) routinely experienced lower percentages ranging from 11 – 27% and 13 –
400 27%. In the final instance, field transitional woodland/shrub (peat soil) and peatbog (wet) had the highest snow density
401 percentages at 42% and 39%, while open area and coniferous forest (mineral soil) were markedly lower at 33% and 32%.

402



404 **Figure 12: Mean and standard deviation (error bars) for snow-to-water-percentage estimates per LULC with field data and EA.**
405 Blank values indicate no field data.

406
407 As with the field averages, for the local scale averages from December to early April there were generally minimal
408 differences in snow density between different land cover types while experiencing greater fluctuations at the end of April with
409 a maximum difference of 14%. The highest snow densities were generally found with open area and more so with peatbog
410 (wet). Peatbog (wet) contained percentages equal or up to 2% higher than peatbog (dry) from December to March. However,
411 in early April they were both equal before reversing in late April with peatbog (dry) at 45% compared to peatbog (wet) at 41%.
412 The lowest values were generally found with broad-leaved forest (mineral soil) and broad-leaved forest (peat soil), which were
413 always either equal or differed by 1%. Coniferous forest (mineral soil) and coniferous forest (peat soil) also tended to have
414 similar values. However, by late April the snow density in the peat soil was 3% higher during that period of rapid snow melt,
415 with coniferous soil (mineral soil) having the lowest snow density at 31%. Average snow density percentage on transitional
416 woodland/shrub (mineral soil) and transitional woodland/shrub (peat soil) were similar with a maximum difference of 2%. A
417 spatial view of the gradual increase in the snow density percentage across the six instances with the rapid rise at the end of
418 April can be seen in Fig 13.



419
420 **Figure 13: Field and estimated snow density percentage in a) 14-December-22, b) 17-January-23, c) 15-February-23, d) 17-March-
421 28-April-23, and f) 28-April-23 alongside g) a LULC map.**

422 **5 Discussion**

423 With snow depth estimation, all models performed well, with CNN, RF, SVM, ANN, and EA all being capable of
424 generating encouraging statistics. As is common for the study region the snow depth was lowest in December and highest in
425 March before daily temperatures began exceeding 0 °C in April. There were consistent differences in snow depth between
426 different vegetative communities. This was most apparent with higher snow depth being associated with broad-leaved forests,
427 transitional woodland/shrubs, and particularly with coniferous forest (peat soil). Shallower snow depth was recorded at
428 coniferous forest (mineral soil), open areas, and both dry and wet peatbogs. With peatbogs, wet peat conducts heat better than
429 dry peat resulting in heat flowing more effortlessly in wet peat layers in winter (Kujala et al., 2008), which may result in

430 increased snowmelt and compaction. Furthermore, mineral soil is more thermally conductive than peat soil (Atchley et al.,
431 2016), which may promote snowmelt and compaction in similar vegetation communities containing mineral soil compared
432 with peat soil where snowmelt and compaction would be reduced. Forests with drier mineral soils were generally more shielded
433 from saturated soil found in peatbogs, while forests with peat soil were oftentimes adjacent to peatbogs. As the water table in
434 many parts was at or near the surface, adjacent soils would contain greater soil saturation while the shielded mineral soils
435 would in theory be more unsaturated. A notable exception is for approximately half of the broad-leaved forest (mineral soil)
436 that is along the Kitinen River, which may have especially influenced snow depth, SWE, and snow density readings for that
437 LULC. Given that saturated soil needs greater energy to heat than does unsaturated soil (Howe and Smith, 2021), saturated
438 soil would require greater energy to warm in the spring and remain warmer in the winter than the unsaturated soil, which would
439 have a resulting impact on snow cover. Post winter soil thaw varied with five FMI Campbell Scientific 109-L soil temperature
440 sensors in the study area at 5 and 10 cm below the surface. For two sensors found in coniferous forest and one in an open area
441 with mineral soil, the soil fully thawed out between 10 – 25 April, while for the two sensors in the peatland, the soil thawed
442 out from 11 – 13 May, which would have aided in accelerating overlaying snow cover melt for the former. It should be noted
443 the impact that direct solar radiation may have on the energy balance of the snowpack and melt processes, along with wind
444 impacted (open areas) versus wind protected (forest) vegetative communities. Lastly, snow interception and sublimation are
445 major factors in forest communities, especially with conifers, which can lead to a notable diversity of snow accumulation on
446 the forest floor (Helbig, 2020).

447 For the SWE estimations, model results were more mixed, but nonetheless promising. SVM, ANN, and EA were all
448 able to produce positive metrics, while there was elevated variation with both CNN and RF. MLR also performed well despite
449 being the simplest form of machine learning in this study. In comparison to the snow depth there was a much smaller sample
450 size which led to greater model uncertainty and disagreement. While the higher snow depth sample size may have benefited
451 more complex models for snow depth modeling, simpler models seemed to perform better with the more limited SWE sample
452 size. A greater number of SWE field samples would have provided enhanced findings; however, these field measurements can
453 be time-consuming and expensive to collect across a large geographic region, with SWE measurements taking approximately
454 20 times as long to complete compared to snow depth measurements (Sturm et al., 2010). Nonetheless SWE was found to be
455 lowest in December and highest in early April, which was post-peak snow depth. With the field data, it was found that SWE
456 was higher in transitional woodland/shrub (peat soil) than with coniferous forest (mineral soil), which may be attributed to
457 potentially more saturated peat soil allowing for greater water retention within the snow cover, while the unsaturated mineral
458 soil drained slightly more liquid from the overlaying snow cover. Mineral soils across the study site are sand-rich and would
459 be dry most of the time at the surface and likely never reach saturation, with any melted snow being drained in these soils. The
460 one exception was with the end of April when there was a notable reversal, which may have been due to increased snow
461 interception, snowmelt, sublimation, and windblown snow from branches in some vegetation types. A similar trend was
462 observed at the local scale. Local scale coniferous forest (peat soil) continually contained higher average SWE than coniferous
463 forest (mineral soil) which may be the result of the unsaturated mineral soil absorbing water from the overlaying snow while

464 the saturated peat soil slowed the draining of water through the snowpack and into the soils. Dry and especially wet peatbogs
465 largely contained the lowest SWE measurements. These low open areas likely experienced enhanced wind activity that blew
466 snow laterally away while also leading to greater sublimation. This would have led to greater snow particle cohesion and
467 denser wind slab layer formation at the surface of the snowpack due to sintering after snow was mobilized in the wind (Mott
468 et al., 2018).

469 Lastly, snow density was lowest in December and increased until the end of April when it was highest, which was
470 during a period of rapid snowmelt. This was to be expected given that the beginning and middle winter typically contain larger
471 quantities of fresh snowfall, while by the end of winter the snowpack would have compacted over time and become denser as
472 the snowpack reaches an equilibrium temperature state of 0 °C (e.g., isothermal). As the snowpack develops, a larger snow
473 grain size (depth hoar) results in a lower density in shallow snowpack. However, as the snowpack becomes isothermal, the
474 depth hoar layer will metamorphose and become denser, especially near the ground (Gu et al., 2019). With the field data, a
475 higher snow density percentage was observed at the end of April in peatbog (wet) and transitional woodland/shrub (peat soil)
476 which contrasted with coniferous forest (mineral soil) and open area and may be attributed to soil saturation for those specific
477 locations. At the end of April for the local scale the highest snow density percentages were found in vegetative communities
478 that were more impacted by wind such as arable along with peatbog (wet) and peatbog (dry). In contrast, both broad-leaved
479 forest and coniferous forest in mineral and peat soils typically had the lowest percentages. Local scale wet peatbog was found
480 to generally contain slightly higher amounts than dry peatbog. This may be attributed to dry peatbog being on average ~2.2 m
481 higher in elevation than wet peatbog in our study area, which may have contributed to the movement of water over time to wet
482 peatbogs at incrementally lower elevations.

483 Solar radiation increased throughout the timeframe and was not uniform over the study area, such as with thick forests
484 sometimes obscuring adjacent canopy-free areas from solar radiation. As this would have impacted real-world snow estimates,
485 we incorporated end of winter WV-2 imagery in the framework as it was able to aid in capturing such irregularities. A limited
486 quantity and spatial extent of field measurements restricted further associations with vegetative communities, especially for
487 SWE and, in turn, snow density. Had additional measurements been taken at communities missing field data, there would be
488 a more comprehensive understanding of snow-landcover relationships. Additional datasets would have likely improved the
489 model statistics and estimation of all three studied features. Soil moisture and air/subsurface temperature data were accessible
490 in the study area yet were excluded, despite their strong association with snow depth and SWE (Contosta et al., 2016). This
491 was due to a limited number of these measurements that corresponded to the six instances, with some containing gaps or
492 missing data which would hinder spatial mapping and association with landcover types. Furthermore, very few of these
493 measurements were located on or adjacent to the field snow depth and SWE measurements, which severely limited a proper
494 linkage between the field data with soil moisture and temperature. Additional remote-sensing based data could have been
495 utilized as an add-on to assist in mapping soil moisture and temperature for the study, alongside improving estimations for
496 snow depth and SWE. However, due to the vegetative heterogeneity at the 10 km² site and clustering of the field data, medium
497 and low-resolution imagery would have provided questionable benefit. High-resolution hyperspectral imagery and Synthetic

498 Aperture Radar (SAR) are particularly relevant, given the additional available spectral bands of the former and the proven
499 application with snow depth and SWE detection in the latter (Patil et al., 2020) and would have likely benefited the findings.

500 The applied model was able to establish connections between remote sensing data and snow measurements to estimate
501 surrounding snow depth, SWE, and snow density over multiple instances. In terms of performance, it was seen with the more
502 numerous field snow depth data that more complex machine learning and a deep learning model could perform well, while in
503 instances of very limited data for SWE, simpler machine models were more prone to succeed. Regardless of the sample size,
504 an ensemble approach of different models was able to perform well in both circumstances whereby it can adapt its effectiveness
505 in the case of changing the output variable and sample size. In terms of model transferability from this effort, in conditions
506 where there are plentiful input data for model training, more complex deep learning and machine learning models should be
507 utilized to better identify intricate patterns. However, if there is a notable training sample size limitation then it may be
508 advisable to utilize uncomplicated models that may be better suited for recognizing trends with the limited data. This added
509 flexibility in the types of base models to be used for such an ensemble approach allows it to be applied to smaller snow-related
510 datasets covering local scale areas, to larger datasets with hundreds or thousands of data points that can cover regional and
511 potentially global scales. In any case, model inputs would need to be appropriately defined regarding the type of terrain and
512 data to be utilized, such as for example field data along mountain ranges compared to low-lying open areas.

513 **6 Conclusions**

514 We employed an object-based hybrid deep learning and machine learning ensemble approach with time-series field
515 snow depth and SWE data in northern Finland to first estimate snow depth at a local scale, before incorporating the snow depth
516 outputs to estimate SWE at the same local scale alongside generating snow density estimations from six instances between
517 December 2022 and April 2023. Snow depth peaked in March, SWE peaked shortly after in early April, and snow density
518 peaked with the final available data at the end of April. Multiple machine learning models, particularly with the ensemble
519 approach, were shown to positively estimate key snowpack attributes over the period at the study site in Sodankylä despite
520 limited field snow depth and SWE observations. We established that there are direct spatial and temporal connections between
521 three commonly studied snowpack elements with vegetation and soil types, with more research recommended to further
522 characterize these associations. Although there is promise with intricate deep learning and machine learning techniques, this
523 study also highlights opportunities to assess where less complex methods may be employed for computational efficiency and
524 performance, especially when scaling up. While performed over a small portion of northern Finland, when matched with other
525 field-based snowpack and remote sensing data across the region it would be possible to further upscale the studied snow-based
526 estimates over a wider, regional-scale over various periods in time. This would also need to account for differing types of
527 snowpack, terrain, and vegetative communities found throughout the pan-Arctic domain. As average temperatures around the
528 Arctic are projected to increase with fewer days below freezing, more uncertain climactic conditions and precipitation events
529 would affect the quantity, rate, and timing of snowfall, snow-on/snow-off, and snowmelt runoff in the region. Given that

530 waterbodies such as lakes, ponds, and rivers in Finland and other high latitude areas are fed by the annual snowmelt, any
531 changes to this natural process would meaningfully alter the hydrological makeup. The hybrid-based methodology applied in
532 this effort can serve to benefit future snow-related analyses in high latitude regions, alongside other areas on Earth that
533 regularly experience seasonal snow.

534 **Appendix A**

535 In this Appendix, we present relevant model hyperparameters utilized in the study. Model parameters remained the
536 same during each of the six instances to ensure fair comparisons, with only the best optimization values being automatically
537 selected.

538 **Table 1: List of model summaries and parameters.**

Model	Description	Parameters	Method in R
Convolutional Neural Network	A neural network that includes at least one convolutional layer. Typically has some combination of convolutional, pooling, and dense layers.	Layer_conv_1d Filters: 32, Kernel_size: 2, Activation: relu, Layer_max_pooling_1d Pool_size: 2 Layer_flatten Layer_dense Units: 64, Activation: relu, Layer_dense units = 32, Activation: relu, Layer_dense units = 1, Activation: linear, Epochs: 100, Batch_size: 4	layer_conv_1d
Random Forest	Combines outputs from a collection of decision trees to generate an optimal output value.	Ntree: 20 Mtry: 1, 2, 3, 4	rf
Support Vector Machine	Relies on an optimal hyperplane that minimizes error bounds and here uses a polynomial kernal.	Degree: 2, 3, C: 0.01, 0.1, 1.0, 10.0, 100.0,	svmPoly

		Scale: 0.05, 0.1, 0.15, 0.2, 0.25, 0.3, 0.35, 0.4
ANN	A feed-forward neural network with a single hidden layer.	Size: Between 2 and 8; increasing by 1, Decay: Between 0.01 and 0.1; increasing by 0.01, Maxit: 200, Abstol: 0.0001
Multiple Linear Regression	Quantifies the linear relationship between multiple independent variables and a dependent variable by finding the best-fitting linear equation.	lm

539 *Code and data availability.* Field snow depth and snow water equivalent data is maintained by the Finnish Meteorological
 540 Institute and is available at <https://litdb.fmi.fi/index.php>. Code used for this manuscript is found at <https://github.com/CRREL->
 541 [David/FMI-SnowDepth-SWE.git](https://github.com/CRREL-David/FMI-SnowDepth-SWE.git) and contains field and remote sensing variables. Additional study data is available upon
 542 reasonable request.

543 *Author contributions.* DB, LVB, EJD, and TAD designed and initiated the study. RRB classified vegetation. EJD obtained
 544 LiDAR data. JL obtained field snow observations. DB, LVB, and EJD developed the methodology. DB wrote the initial draft
 545 and figures. All authors contributed to manuscript development and review.

546 *Competing interests.* The authors declare that they have no conflict of interest.

547 *Acknowledgements.* Staff at the Finnish Meteorological Institute are acknowledged for providing field measurements.

548 *Financial support.* This research was funded by the US Department of Defense - PE 0602144A Program Increase 'Defense
 549 Resiliency Platform Against Extreme Cold Weather'.

550 **References**

551 Anttila, K., Manninen, T., Karjalainen, T., Lahtinen, P., Riihelä, A., and Siljamo, N.: The temporal and spatial variability in
 552 submeter scale surface roughness of seasonal snow in Sodankylä Finnish Lapland in 2009–2010, *JGR Atmospheres*,
 553 119, 9236–9252, doi:10.1002/2014JD021597, 2014.

554 Arenson, L., Colgan, W., and Marshall, H. P.: Physical, thermal, and mechanical properties of snow, ice, and permafrost, in:
555 Snow and Ice-Related Hazards, Risks, and Disasters, Elsevier, 35–71, doi:10.1016/B978-0-12-817129-5.00007-X,
556 2021.

557 Atchley, A. L., Coon, E. T., Painter, S. L., Harp, D. R., and Wilson, C. J.: Influences and interactions of inundation, peat, and
558 snow on active layer thickness, *Geophysical Research Letters*, 43, 5116–5123, doi:10.1002/2016GL068550, 2016.

559 Aune-Lundberg, L. and Strand, G.-H.: The content and accuracy of the CORINE Land Cover dataset for Norway, *International*
560 *Journal of Applied Earth Observation and Geoinformation*, 96, 102266, doi:10.1016/j.jag.2020.102266, 2021.

561 Bai, J., Heikkilä, A., and Zong, X.: Long-Term Variations of Global Solar Radiation and Atmospheric Constituents at
562 Sodankylä in the Arctic, *Atmosphere*, 12, 749, doi:10.3390/atmos12060749, 2021.

563 Bair, E. H., Abreu Calfa, A., Rittger, K., and Dozier, J.: Using machine learning for real-time estimates of snow water
564 equivalent in the watersheds of Afghanistan, *The Cryosphere*, 12, 1579–1594, doi:10.5194/tc-12-1579-2018, 2018.

565 Barnett, T. P., Adam, J. C., and Lettenmaier, D. P.: Potential impacts of a warming climate on water availability in snow-
566 dominated regions, *Nature*, 438, 303–309, doi:10.1038/nature04141, 2005.

567 Bartsch, A., Bergstedt, H., Pointner, G., Muri, X., Rautiainen, K., Leppänen, L., Joly, K., Sokolov, A., Orekhov, P., Ehrich,
568 D., and Soininen, E. M.: Towards long-term records of rain-on-snow events across the Arctic from satellite data, *The*
569 *Cryosphere*, 17, 889–915, doi:10.5194/tc-17-889-2023, 2023.

570 Bösinger, T.: The Geophysical Observatory in Sodankylä, Finland – past and present, *Hist. Geo Space. Sci.*, 12, 115–130,
571 doi:10.5194/hgss-12-115-2021, 2021.

572 Brodylo, D., Douglas, T. A., and Zhang, C.: Quantification of active layer depth at multiple scales in Interior Alaska
573 permafrost, *Environ. Res. Lett.*, 19, 034013, doi:10.1088/1748-9326/ad264b, 2024.

574 Brown, R. D., Smith, C., Derksen, C., and Mudryk, L.: Canadian In Situ Snow Cover Trends for 1955–2017 Including an
575 Assessment of the Impact of Automation, *Atmosphere-Ocean*, 59, 77–92, doi:10.1080/07055900.2021.1911781,
576 2021.

577 Broxton, P. D., Van Leeuwen, W. J. D., and Biederman, J. A.: Improving Snow Water Equivalent Maps With Machine
578 Learning of Snow Survey and Lidar Measurements, *Water Resources Research*, 55, 3739–3757,
579 doi:10.1029/2018WR024146, 2019.

580 Cammalleri, C., Barbosa, P., and Vogt, J. V.: Testing remote sensing estimates of snow water equivalent in the framework of
581 the European Drought Observatory, *J. Appl. Rem. Sens.*, 16, doi:10.11117/1.JRS.16.014509, 2022.

582 Cimoli, E., Marcer, M., Vandecrux, B., Bøggild, C. E., Williams, G., and Simonsen, S. B.: Application of Low-Cost UASs
583 and Digital Photogrammetry for High-Resolution Snow Depth Mapping in the Arctic, *Remote Sensing*, 9, 1144,
584 doi:10.3390/rs9111144, 2017.

585 Collados-Lara, A.-J., Pulido-Velazquez, D., Pardo-Igúzquiza, E., and Alonso-González, E.: Estimation of the spatiotemporal
586 dynamic of snow water equivalent at mountain range scale under data scarcity, *Science of The Total Environment*,
587 741, 140485, doi:10.1016/j.scitotenv.2020.140485, 2020.

588 Colliander, A., Mousavi, M., Kimball, J. S., Miller, J. Z., and Burgin, M.: Spatial and temporal differences in surface and
589 subsurface meltwater distribution over Greenland ice sheet using multi-frequency passive microwave observations,
590 *Remote Sensing of Environment*, 295, 113705, doi:10.1016/j.rse.2023.113705, 2023.

591 Contosta, A. R., Burakowski, E. A., Varner, R. K., and Frey, S. D.: Winter soil respiration in a humid temperate forest: The
592 roles of moisture, temperature, and snowpack, *JGR Biogeosciences*, 121, 3072–3088, doi:10.1002/2016JG003450,
593 2016.

594 Deems, J. S., Painter, T. H., and Finnegan, D. C.: Lidar measurement of snow depth: a review, *J. Glaciol.*, 59, 467–479,
595 doi:10.3189/2013JoG12J154, 2013.

596 Douglas, T. A. and Zhang, C.: Machine learning analyses of remote sensing measurements establish strong relationships
597 between vegetation and snow depth in the boreal forest of Interior Alaska, *Environ. Res. Lett.*, 16, 065014,
598 doi:10.1088/1748-9326/ac04d8, 2021.

599 Duan, S., Ullrich, P., Risser, M., and Rhoades, A.: Using Temporal Deep Learning Models to Estimate Daily Snow Water
600 Equivalent Over the Rocky Mountains, *Water Resources Research*, 60, doi:10.1029/2023wr035009, 2024.

601 El Oufir, M. K., Chokmani, K., El Alem, A., Agili, H., and Bernier, M.: Seasonal Snowpack Classification Based on Physical
602 Properties Using Near-Infrared Proximal Hyperspectral Data, *Sensors*, 21, 5259, doi:10.3390/s21165259, 2021.

603 Essery, R., Kontu, A., Lemmettyinen, J., Dumont, M., and Ménard, C. B.: A 7-year dataset for driving and evaluating snow
604 models at an Arctic site (Sodankylä, Finland), *Geosci. Instrum. Method. Data Syst.*, 5, 219–227, doi:10.5194/gi-5-
605 219-2016, 2016.

606 FMI (Finnish Meteorological Institute): Weather and sea database, available at: <https://en.ilmatieteenlaitos.fi/download-observations>, last accessed 14 December, 2024.

607 Fontrodona-Bach, A., Schaeffli, B., Woods, R., Teuling, A. J., and Larsen, J. R.: NH-SWE: Northern Hemisphere Snow Water
608 Equivalent dataset based on in situ snow depth time series, *Earth Syst. Sci. Data*, 15, 2577–2599, doi:10.5194/essd-
610 15-2577-2023, 2023.

611 Gaitán, J. J., Bran, D., Oliva, G., Ciari, G., Nakamatsu, V., Salomone, J., Ferrante, D., Buono, G., Massara, V., Humano, G.,
612 Celdrán, D., Opazo, W., and Maestre, F. T.: Evaluating the performance of multiple remote sensing indices to predict
613 the spatial variability of ecosystem structure and functioning in Patagonian steppes, *Ecological Indicators*, 34, 181–
614 191, doi:10.1016/j.ecolind.2013.05.007, 2013.

615 Goldberg, K., Herrmann, I., Hochberg, U., and Rozenstein, O.: Generating Up-to-Date Crop Maps Optimized for Sentinel-2
616 Imagery in Israel, *Remote Sensing*, 13, 3488, doi:10.3390/rs13173488, 2021.

617 Green, J., Kongoli, C., Prakash, A., Sturm, M., Duguay, C., and Li, S.: Quantifying the relationships between lake fraction,
618 snow water equivalent and snow depth, and microwave brightness temperatures in an arctic tundra landscape, *Remote
619 Sensing of Environment*, 127, 329–340, doi:10.1016/j.rse.2012.09.008, 2012.

620 Gu, L., Fan, X., Li, X., and Wei, Y.: Snow Depth Retrieval in Farmland Based on a Statistical Lookup Table from Passive
621 Microwave Data in Northeast China, *Remote Sensing*, 11, 3037, doi:10.3390/rs11243037, 2019.

622 Helbig, N., Moeser, D., Teich, M., Vincent, L., Lejeune, Y., Sicart, J.-E., and Monnet, J.-M.: Snow processes in mountain
623 forests: interception modeling for coarse-scale applications, *Hydrol. Earth Syst. Sci.*, 24, 2545–2560,
624 doi:10.5194/hess-24-2545-2020, 2020.

625 Henkel, P., Koch, F., Appel, F., Bach, H., Prasch, M., Schmid, L., Schweizer, J., and Mauser, W.: Snow Water Equivalent of
626 Dry Snow Derived From GNSS Carrier Phases, *IEEE Trans. Geosci. Remote Sensing*, 56, 3561–3572,
627 doi:10.1109/TGRS.2018.2802494, 2018.

628 Hoopes, C. A., Castro, C. L., Behrangi, A., Ehsani, M. R., and Broxton, P.: Improving prediction of mountain snowfall in the
629 southwestern United States using machine learning methods, *Meteorological Applications*, 30, e2153,
630 doi:10.1002/met.2153, 2023.

631 Howe, J. A. and Smith, A. P.: The soil habitat, in: *Principles and Applications of Soil Microbiology*, Elsevier, 23–55,
632 doi:10.1016/B978-0-12-820202-9.00002-2, 2021.

633 Hu, Y., Che, T., Dai, L., Zhu, Y., Xiao, L., Deng, J., and Li, X.: A long-term daily gridded snow depth dataset for the Northern
634 Hemisphere from 1980 to 2019 based on machine learning, *Big Earth Data*, 1–28,
635 doi:10.1080/20964471.2023.2177435, 2023.

636 Jacobs, J. M., Hunsaker, A. G., Sullivan, F. B., Palace, M., Burakowski, E. A., Herrick, C., and Cho, E.: Snow depth mapping
637 with unpiloted aerial system lidar observations: a case study in Durham, New Hampshire, United States, *The
638 Cryosphere*, 15, 1485–1500, doi:10.5194/tc-15-1485-2021, 2021.

639 Jonas, T., Marty, C., and Magnusson, J.: Estimating the snow water equivalent from snow depth measurements in the Swiss
640 Alps, *Journal of Hydrology*, 378, 161–167, doi:10.1016/j.jhydrol.2009.09.021, 2009.

641 Kelly, R. E., Chang, A. T., Tsang, L., and Foster, J. L.: A prototype AMSR-E global snow area and snow depth algorithm,
642 *IEEE Trans. Geosci. Remote Sensing*, 41, 230–242, doi:10.1109/TGRS.2003.809118, 2003.

643 Kesikoglu, M. H.: Enhancing Snow Detection through Deep Learning: Evaluating CNN Performance Against Machine
644 Learning and Unsupervised Classification Methods, *Water Resour Manage*, doi:10.1007/s11269-025-04240-4, 2025.

645 King, F., Erler, A. R., Frey, S. K., and Fletcher, C. G.: Application of machine learning techniques for regional bias correction
646 of snow water equivalent estimates in Ontario, Canada, *Hydrol. Earth Syst. Sci.*, 24, 4887–4902, doi:10.5194/hess-
647 24-4887-2020, 2020.

648 King, F., Kelly, R., and Fletcher, C. G.: New opportunities for low-cost LiDAR-derived snow depth estimates from a consumer
649 drone-mounted smartphone, *Cold Regions Science and Technology*, 207, 103757,
650 doi:10.1016/j.coldregions.2022.103757, 2023.

651 Kongoli, C., Key, J., and Smith, T.: Mapping of Snow Depth by Blending Satellite and In-Situ Data Using Two-Dimensional
652 Optimal Interpolation—Application to AMSR2, *Remote Sensing*, 11, 3049, doi:10.3390/rs11243049, 2019.

653 Kujala, K., Seppälä, M., and Holappa, T.: Physical properties of peat and palsu formation, *Cold Regions Science and
654 Technology*, 52, 408–414, doi:10.1016/j.coldregions.2007.08.002, 2008.

655 Leppänen, L., Kontu, A., Hannula, H.-R., Sjöblom, H., and Pulliainen, J.: Sodankylä manual snow survey program, *Geosci. Instrum. Method. Data Syst.*, 5, 163–179, doi:10.5194/gi-5-163-2016, 2016.

656

657 Leppänen, L., Kontu, A., and Pulliainen, J.: Automated Measurements of Snow on the Ground in Sodankylä, *Geophysica*, 53, 45–64, 2018.

658

659 Li, K., DeCost, B., Choudhary, K., Greenwood, M., and Hattrick-Simpers, J.: A critical examination of robustness and 660 generalizability of machine learning prediction of materials properties, *npj Comput Mater*, 9, 55, doi:10.1038/s41524- 661 023-01012-9, 2023.

662 Li, Y., Luo, T., and Ma, C.: Nonlinear Weighted Directed Acyclic Graph and A Priori Estimates for Neural Networks, *SIAM 663 Journal on Mathematics of Data Science*, 4, 694–720, doi:10.1137/21m140955x, 2022.

664 Liljestrand, D., Johnson, R., Skiles, S. M., Burian, S., and Christensen, J.: Quantifying regional variability of machine-learning- 665 based snow water equivalent estimates across the Western United States, *Environmental Modelling & Software*, 177, 106053, doi:10.1016/j.envsoft.2024.106053, 2024.

666

667 Lu, X., Hu, Y., Zeng, X., Stamnes, S. A., Neuman, T. A., Kurtz, N. T., Yang, Y., Zhai, P.-W., Gao, M., Sun, W., Xu, K., Liu, 668 Z., Omar, A. H., Baize, R. R., Rogers, L. J., Mitchell, B. O., Stamnes, K., Huang, Y., Chen, N., Weimer, C., Lee, J., 669 and Fair, Z.: Deriving Snow Depth From ICESat-2 Lidar Multiple Scattering Measurements: Uncertainty Analyses, 670 *Front. Remote Sens.*, 3, 891481, doi:10.3389/frsen.2022.891481, 2022.

671 Marti, R., Gascoin, S., Berthier, E., De Pinel, M., Houet, T., and Laffly, D.: Mapping snow depth in open alpine terrain from 672 stereo satellite imagery, *The Cryosphere*, 10, 1361–1380, doi:10.5194/tc-10-1361-2016, 2016.

673 Meinander, O., Kontu, A., Kouznetsov, R., and Sofiev, M.: Snow Samples Combined With Long-Range Transport Modeling 674 to Reveal the Origin and Temporal Variability of Black Carbon in Seasonal Snow in Sodankylä (67°N), *Front. Earth 675 Sci.*, 8, 153, doi:10.3389/feart.2020.00153, 2020.

676 Mott, R., Vionnet, V., and Grünewald, T.: The Seasonal Snow Cover Dynamics: Review on Wind-Driven Coupling Processes, 677 *Front. Earth Sci.*, 6, 197, doi:10.3389/feart.2018.00197, 2018.

678 Muskett, R. R.: Remote Sensing, Model-Derived and Ground Measurements of Snow Water Equivalent and Snow Density in 679 Alaska, *IJG*, 03, 1127–1136, doi:10.4236/ijg.2012.35114, 2012.

680 Nagler, T. and Rott, H.: Retrieval of wet snow by means of multitemporal SAR data, *IEEE Trans. Geosci. Remote Sensing*, 681 38, 754–765, doi:10.1109/36.842004, 2000.

682 Nadjla, B., Assia, S., and Ahmed, Z.: Contribution of spectral indices of chlorophyll (RECI and GCI) in the analysis of multi- 683 temporal mutations of cultivated land in the Mostaganem plateau, in: 2022 7th International Conference on Image and 684 Signal Processing and their Applications (ISPA), 2022 7th International Conference on Image and Signal Processing and 685 their Applications (ISPA), Mostaganem, Algeria, 1–6, doi:10.1109/ISPA54004.2022.9786326, 2022.

686 Nienow, P. W. and Campbell, F.: Stratigraphy of Snowpacks, in: *Encyclopedia of Snow, Ice and Glaciers*, edited by: Singh, 687 V. P., Singh, P., and Haritashya, U. K., Springer Netherlands, Dordrecht, 1081–1084, doi:10.1007/978-90-481-2642- 688 2_541, 2011.

689 Nijhawan, R., Das, J., and Raman, B.: A hybrid of deep learning and hand-crafted features based approach for snow cover
690 mapping, *International Journal of Remote Sensing*, 40, 759–773, doi:10.1080/01431161.2018.1519277, 2019.

691 Nolin, A. W.: Recent advances in remote sensing of seasonal snow, *J. Glaciol.*, 56, 1141–1150,
692 doi:10.3189/002214311796406077, 2010.

693 Ntokas, K. F. F., Odry, J., Boucher, M.-A., and Garnaud, C.: Investigating ANN architectures and training to estimate snow
694 water equivalent from snow depth, *Hydrol. Earth Syst. Sci.*, 25, 3017–3040, doi:10.5194/hess-25-3017-2021, 2021.

695 Pan, J., Durand, M. T., Vander Jagt, B. J., and Liu, D.: Application of a Markov Chain Monte Carlo algorithm for snow water
696 equivalent retrieval from passive microwave measurements, *Remote Sensing of Environment*, 192, 150–165,
697 doi:10.1016/j.rse.2017.02.006, 2017.

698 Patil, A., Singh, G., and Rüdiger, C.: Retrieval of Snow Depth and Snow Water Equivalent Using Dual Polarization SAR Data,
699 *Remote Sensing*, 12, 1183, doi:10.3390/rs12071183, 2020.

700 Pes, B.: Ensemble feature selection for high-dimensional data: a stability analysis across multiple domains, *Neural Comput &*
701 *Appl.*, 32, 5951–5973, doi:10.1007/s00521-019-04082-3, 2020.

702 Prowse, T. D. and Owens, I. F.: Characteristics of Snowfalls, Snow Metamorphism, and Snowpack Structure with Implications
703 for Avalanching, Craigieburn Range, New Zealand, *Arctic and Alpine Research*, 16, 107, doi:10.2307/1551176, 1984.

704 Pulliainen, J., Luojus, K., Derksen, C., Mudryk, L., Lemmetyinen, J., Salminen, M., Ikonen, J., Takala, M., Cohen, J.,
705 Smolander, T., and Norberg, J.: Patterns and trends of Northern Hemisphere snow mass from 1980 to 2018, *Nature*,
706 581, 294–298, doi:10.1038/s41586-020-2258-0, 2020.

707 Raghubanshi, S., Agrawal, R., and Rathore, B. P.: Enhanced snow cover mapping using object-based classification and
708 normalized difference snow index (NDSI), *Earth Sci Inform*, 16, 2813–2824, doi:10.1007/s12145-023-01077-6,
709 2023.

710 Rautiainen, K., Lemmetyinen, J., Schwank, M., Kontu, A., Ménard, C. B., Mätzler, C., Drusch, M., Wiesmann, A., Ikonen, J.,
711 and Pulliainen, J.: Detection of soil freezing from L-band passive microwave observations, *Remote Sensing of*
712 *Environment*, 147, 206–218, doi:10.1016/j.rse.2014.03.007, 2014.

713 Rodell, M. and Houser, P. R.: Updating a Land Surface Model with MODIS-Derived Snow Cover, *Journal of*
714 *Hydrometeorology*, 5, 1064–1075, doi:10.1175/JHM-395.1, 2004.

715 Salzmann, N., Huggel, C., Rohrer, M., and Stoffel, M.: Data and knowledge gaps in glacier, snow and related runoff research
716 – A climate change adaptation perspective, *Journal of Hydrology*, 518, 225–234, doi:10.1016/j.jhydrol.2014.05.058,
717 2014.

718 Santi, E., Brogioni, M., Leduc-Leballeur, M., Macelloni, G., Montomoli, F., Pampaloni, P., Lemmetyinen, J., Cohen, J., Rott,
719 H., Nagler, T., Derksen, C., King, J., Rutter, N., Essery, R., Menard, C., Sandells, M., and Kern, M.: Exploiting the
720 ANN Potential in Estimating Snow Depth and Snow Water Equivalent From the Airborne SnowSAR Data at X- and
721 Ku-Bands, *IEEE Trans. Geosci. Remote Sensing*, 60, 1–16, doi:10.1109/TGRS.2021.3086893, 2022.

722 Santry, D. J.: Convolutional Neural Networks, in: Demystifying Deep Learning, Wiley, 111–131,
723 doi:10.1002/9781394205639.ch6, 2023.

724 Seibert, J., Jenicek, M., Huss, M., and Ewen, T.: Snow and Ice in the Hydrosphere, in: Snow and Ice-Related Hazards, Risks,
725 and Disasters, Elsevier, 99–137, doi:10.1016/B978-0-12-394849-6.00004-4, 2015.

726 Shao, D., Li, H., Wang, J., Hao, X., Che, T., and Ji, W.: Reconstruction of a daily gridded snow water equivalent product for
727 the land region above 45° N based on a ridge regression machine learning approach, *Earth Syst. Sci. Data*, 14, 795–
728 809, doi:10.5194/essd-14-795-2022, 2022.

729 Stillinger, T., Rittger, K., Raleigh, M. S., Michell, A., Davis, R. E., and Bair, E. H.: Landsat, MODIS, and VIIRS snow cover
730 mapping algorithm performance as validated by airborne lidar datasets, *The Cryosphere*, 17, 567–590, doi:10.5194/tc-
731 17-567-2023, 2023.

732 Sturm, M., Taras, B., Liston, G. E., Derksen, C., Jonas, T., and Lea, J.: Estimating Snow Water Equivalent Using Snow Depth
733 Data and Climate Classes, *Journal of Hydrometeorology*, 11, 1380–1394, doi:10.1175/2010JHM1202.1, 2010.

734 Tanniru, S. and Ramsankaran, R.: Passive Microwave Remote Sensing of Snow Depth: Techniques, Challenges and Future
735 Directions, *Remote Sensing*, 15, 1052, doi:10.3390/rs15041052, 2023.

736 Tsai, Y.-L. S., Dietz, A., Oppelt, N., and Kuenzer, C.: Remote Sensing of Snow Cover Using Spaceborne SAR: A Review,
737 *Remote Sensing*, 11, 1456, <https://doi.org/10.3390/rs11121456>, 2019.

738 Tuttle, S. E. and Jacobs, J. M.: Enhanced Identification of Snow Melt and Refreeze Events From Passive Microwave Brightness
739 Temperature Using Air Temperature, *Water Resources Research*, 55, 3248–3265, doi:10.1029/2018WR023995,
740 2019.

741 Vafakhah, M., Nasiri Khiavi, A., Janizadeh, S., and Ganjhanlo, H.: Evaluating different machine learning algorithms for
742 snow water equivalent prediction, *Earth Sci Inform*, 15, 2431–2445, doi:10.1007/s12145-022-00846-z, 2022.

743 Venäläinen, P., Luojuus, K., Mortimer, C., Lemmetyinen, J., Pulliainen, J., Takala, M., Moisander, M., and Zschenderlein, L.:
744 Implementing spatially and temporally varying snow densities into the GlobSnow snow water equivalent retrieval,
745 *The Cryosphere*, 17, 719–736, doi:10.5194/tc-17-719-2023, 2023.

746 Xing, D., Hou, J., Huang, C., and Zhang, W.: Estimation of Snow Depth from AMSR2 and MODIS Data based on Deep
747 Residual Learning Network, *Remote Sensing*, 14, 5089, doi:10.3390/rs14205089, 2022.

748 Xu, Y., Jones, A., and Rhoades, A.: A quantitative method to decompose SWE differences between regional climate models
749 and reanalysis datasets, *Sci Rep*, 9, 16520, doi:10.1038/s41598-019-52880-5, 2019.

750 Xue, J. and Su, B.: Significant Remote Sensing Vegetation Indices: A Review of Developments and Applications, *Journal of
751 Sensors*, 2017, 1–17, doi:10.1155/2017/1353691, 2017.

752 Yang, J., Jiang, L., Luojuus, K., Pan, J., Lemmetyinen, J., Takala, M., and Wu, S.: Snow depth estimation and historical data
753 reconstruction over China based on a random forest machine learning approach, *The Cryosphere*, 14, 1763–1778,
754 doi:10.5194/tc-14-1763-2020, 2020.

755 Yu, M.-Y., Vasudevan, R., and Johnson-Roberson, M.: LiSnowNet: Real-time Snow Removal for LiDAR Point Cloud,
756 doi:10.48550/ARXIV.2211.10023, 2022.

757 Zhang, J., Pohjola, V. A., Pettersson, R., Norell, B., Marchand, W.-D., Clemenzi, I., and Gustafsson, D.: Improving the
758 snowpack monitoring in the mountainous areas of Sweden from space: a machine learning approach, *Environ. Res.*
759 *Lett.*, 16, 084007, doi:10.1088/1748-9326/abfe8d, 2021.

760 Zhao, W., Mu, C., Han, L., Sun, W., Sun, Y., and Zhang, T.: Spatial and temporal variability in snow density across the
761 Northern Hemisphere, *CATENA*, 232, 107445, doi:10.1016/j.catena.2023.107445, 2023.